UNDERSTANDING AND CONTROL OF POINT DEFECT POPULATIONS IN LITHIUM TANTALATE

By

Jacob M. Ivy

A thesis submitted to the Faculty and the Board of Trustees of the Colorado School of Mines in partial fulfillment of the requirements for the degree of Doctor of Philosophy (Materials Science).

Golden, Colorado

Date _____

Signed: _____
Jacob M. Ivy

Signed: _____
Dr. Geoff L. Brennecka
Thesis Advisor

Golden, Colorado

Date _____

Signed: _____
Dr. Eric Toberer
Associate Professor and Materials Science Program Chair
Materials Science Program

ABSTRACT

Lithium tantalate ($LiTaO_3$, LT) is a ferroelectric material that is used in single crystal form for a variety of electro-optic, nonlinear optic, photo-refractive, and acoustic devices and applications. Commercial $LiTaO_3$ single crystals are grown at a congruently melting composition which is lithium deficient, resulting in the formation of point defect complexes of lithium vacancies (V_{Li}') and tantalum antisite ions (Ta_{Li}''''). These defects play an important role in material properties such as Curie temperature (T_C), ferroelectric coercive field, and thermal conductivity.

Removing the intrinsic point defect clusters in $LiTaO_3$ requires extensive thermal treatment in Li_2O-rich atmospheres, the fundamentals of which are poorly understood. In this thesis, diffusion coefficients of lithium are measured via Raman spectroscopy to provide insight into the vapor transport equilibration (VTE) process that supplies lithium to lithium-deficient $LiTaO_3$. This information is used to develop a sample set of single crystals possessing different concentrations of V_{Li}' and Ta_{Li}'''' clusters to quantify the effects of such defect clusters on acoustic phonon velocity and thermal conductivity. Acoustic velocities measured by inelastic neutron diffraction and ultrasonic transducers indicate that increasing point defect concentrations increase acoustic velocity. Thermoreflectance measurements show that thermal conductivity decreases by a factor of 2 between stoichiometric and congruent $LiTaO_3$ crystals as point defect populations increase.

Polycrystalline $LiTaO_3$ fabrication, something not yet commercially accessible and rarely demonstrated in the literature, is also undertaken. Successful sintering of $LiTaO_3$ is hindered by an anisotropic coefficient of thermal expansion (CTE) and by ionic species with large differences in mobility and volatility. Informed by our work on Li_2O diffusion in single crystals and guided by thermodynamic calculations from collaborators, we demonstrate the first pressureless sintering of single-phase $LiTaO_3$ to up to 95% relative density. We also take initial steps towards using Templated Grain Growth to mitigate CTE-induced stresses in sintered polycrystalline $LiTaO_3$.

TABLE OF CONTENTS

LIST OF FIGURES

LIST OF TABLES

CHAPTER ONE

INTRODUCTION

Imperfections in crystalline materials span a wide range of scale, from the atomic scale, such as point defects, to the micro scale, such as dislocations, to the macroscale, such as free surfaces. Oftentimes, defects play a crucial role in material properties and are tailored to control such properties. Other times, however, the role of defects in regard to material properties are difficult to isolate and these relationships are ambiguously defined. The motivation behind this PhD is to attempt to identify and quantify the effects of a range of defect types on the material phenomenon known as ferroelectric switching. This work seeks to accomplish this goal by developing well-defined and controlled defect populations in a model ferroelectric system that can later be used to separate contributions to switching between defects across six orders of magnitude in size, from atomic vacancies to grain boundary volume.

1.1 Motivation

Since the discovery of ferroelectricity in the 1920's with Rochelle salt,[1] ferroelectric materials have paved the way for development of sonar, ultrasound imaging, infrared detectors, light processors, and many other devices. These technologies depend on the ability to reorient the polar axis of the ferroelectric with an applied electric field. The fundamental details of the polarization reorientation process are still not fully understood, however, particularly in relation to how material defects and interfaces such as atomic scale point defects, grain boundaries and electrode interfaces, porosity and sample surfaces, and so on, affect domain wall pinning and domain nucleation phenomena (which will be further discussed in Chapter 1.1.1). Focusing on a materials system with only two possible polarization directions that is readily available in single crystal form and possesses a relatively straightforward point defect scheme should help to minimize applicable variables and enable a more robust understanding of the effects of point defects on domain wall nucleation and pinning. Such studies could then be systematically extended to exploring the effects of grain boundaries on polarization reversal if polycrystalline samples of the same chemistry could be fabricated.

This thesis is devoted to laying the groundwork for fabrication of sample sets that could address such questions in subsequent studies. In particular, this work develops an improved understanding of intrinsic point defect population control in lithium tantalate ($LiTaO_3$, LT) and leverages this understanding to take important first steps towards the fabrication of dense polycrystalline LT.

1.1.1 Fundamentals of Ferroelectrics and Switching

Ferroelectrics (FEs) are a subset of pyroelectric materials (polar crystals whose spontaneous polarization changes as a function of temperature) whose intrinsic dipole can be reoriented via an external electric field. The net polarization of a ferroelectric can be reset to zero through a variety of mechanisms, but the most common is by heating the material past its Curie temperature, T_C, whereupon it will undergo a phase transformation to a centrosymmetric form that can no longer maintain a spontaneous dipole. Once the part is cooled below T_C, local regions of dipoles with a common polarization vector, called domains, form to both minimize surface charge and, in some systems, to reduce internal mechanical stresses. Boundaries between domains are called domain walls; purely ferroelectric (180°) walls are typically three to five unit cells in thickness,[2] although domain walls that are both ferroelectric and ferroelastic (non-180°) can be significantly larger.[3–5]

The polarization reversal process in ferroelectrics proceeds via domain nucleation and growth. New domains with a polarization vector closely aligned with the applied electric field nucleate at locations of electric field amplification, such as surfaces, point defects, or inclusions.[6–10] Domains that are well-aligned with the external field then grow at the expense of less-well-aligned domains. This necessitates that domain walls are mobile to some extent, which in turn means that they will eventually encounter crystallographic defects. A schematic of domain nucleation and growth in an ideal system, a uniformly-poled single crystal with two possible polar directions along the thickness of the crystal, is shown in Figure 1.1. Switching in polycrystalline ferroelectrics follows similar phenomena, but full polarization magnitudes are more limited due to grain orientations that do not perfectly align with an applied electric field, forcing a fraction of polarization vectors to be aligned out-of-plane. Figure 1.2, modeled after Moulson and Herbert,[11]

exemplifies this in a system containing hexagonal grains with random orientations and a polydomain structure consisting of ferroelastic domain walls.

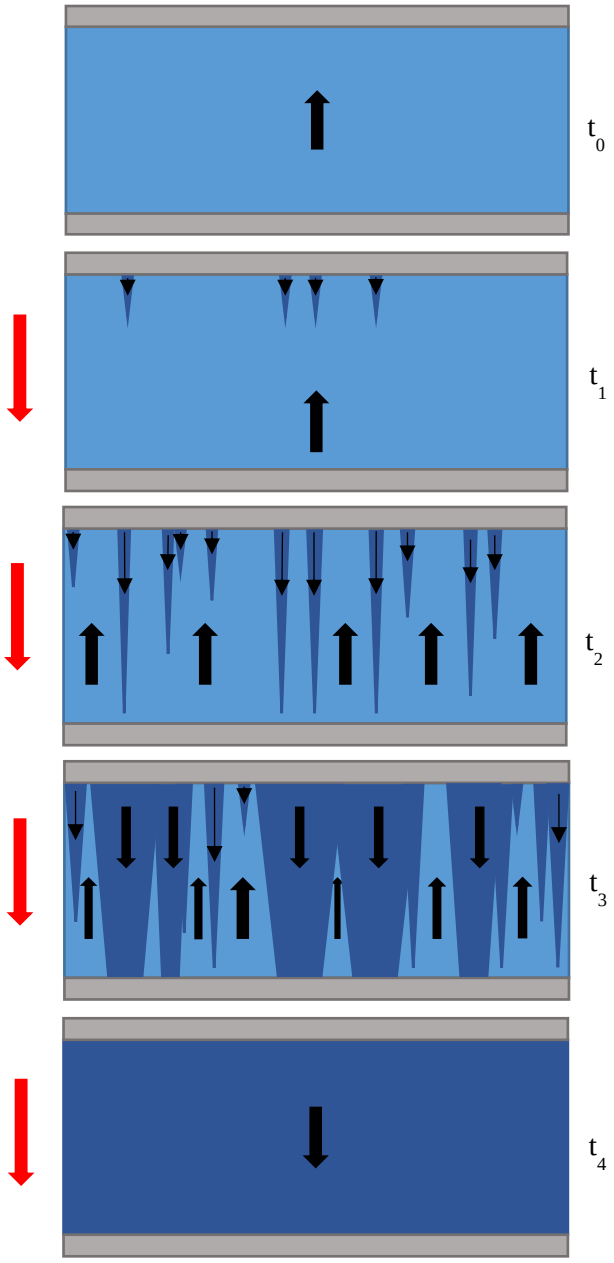

Figure 1.1: (t_0) An ideal single domain with a polarization vector defined by the direction of cation displacement and signified by the black arrow in a single crystal, (t_1) an electric field (red arrows) is applied, and new domains that have a polar vector 180° opposite the existing domain structure nucleate at the interface between the ferroelectric and top electrode, (t_2) & (t_3) favorably-oriented domains grow rapidly through the thickness of the crystal and relatively slowly in the lateral direction while new domains continue to nucleate, (t_4) full polarization reversal is achieved.

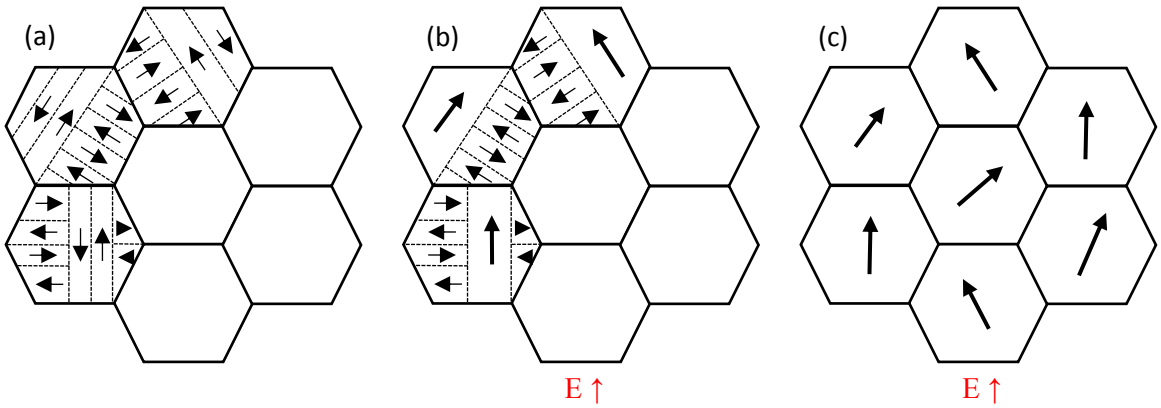

Figure 1.2: (a) A randomly oriented polycrystalline microstructure of hexagonal grains, each of which contains ferroelectric domains that have formed to reduce stress and surface charge. The blank grains in (a) and (b) possess similar domain structures to those enumerated in this figure. (b) An electric field is applied and 180° domains begin switching, resulting in a net polarization. (c) Continued application of higher magnitude electric fields results in polarization redirection of 90° domains and completes the switching process.

The same considerations that make defects preferable for nucleation sites (differences in local structure through chemical or physical changes) can also mean that the same defect may act as a domain wall pinning site, which can again be treated as analogous to grain growth phenomena, specifically that of grain boundary pinning by defects.[7,8,12–14] Pinning of domain walls can be overcome (depinning) through the continued application of larger electric fields until the energy barrier to propagation is surpassed. At the macroscopic scale, this manifests as an overall slowing of the switching process at a given driving force and/or an increase in the driving force required to initiate switching. A schematic of defect-controlled domain nucleation and domain wall propagation is given in Figure 1.3, indicating the difficulty in judging the role(s) of various defects in the switching process. The ambiguous role that defects play in the switching process serves as inspiration for this thesis: under what conditions do specific crystallographic defects act as either domain nucleation or domain wall pinning sites? Understanding nucleation and pinning phenomena is crucial to improving the performance of ferroelectric and piezoelectric materials in a wide array of applications and, unfortunately, these processes are rather poorly differentiated despite seven decades of sustained interest. In large part this is due to the historic difficulty of separating the two mechanisms when measuring dynamic switching of ferroelectrics.

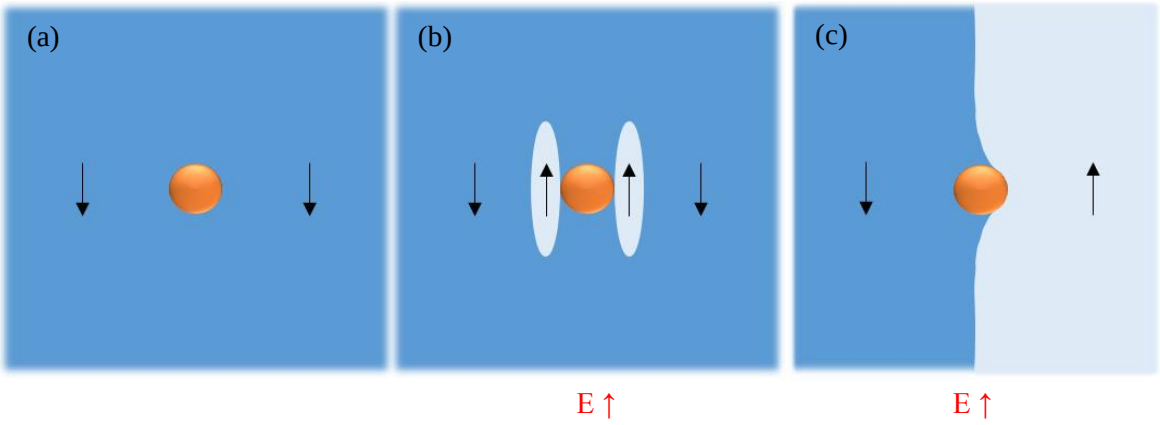

Figure 1.3: (a) An ideal domain, with polarization vectors specified by the black arrows, containing a defect that may be an atomistic (interstitial atom, vacancy, substitutional foreign atom, etc.) or bulk (pore, inclusion of a commensurate or incommensurate particle, etc.) defect in nature. b) Application of an electric field results in the formation of new domains aligned antiparallel with the original polarization vector at the defect site. The energy barrier for nucleation could be lowered at the defect for a variety of reasons: local magnification of the electric field due to permittivity mismatch and lattice strain being just two possibilities. c) A nucleation event occurs elsewhere and a propagating domain wall is pinned by the unknown defect in similar situations that may cause domain nucleation.

1.1.2 Current Understanding of Defect-Domain Wall Interactions

Systematic investigations of domain wall velocity began with Merz in the early 1950's when he established the well-known empirical law, given in Equation 1.1, that has been used to describe the velocity of a propagating domain wall in relation to an applied electric field within bulk ferroelectrics over the intervening decades.[4,15–17]

$$v \propto \exp\left(-\frac{E_a}{E}\right) \tag{1.1}$$

In this equation, shown graphically in Figure 1.4, v represents the domain wall velocity, E is the magnitude of the applied electric field, and E_a is the "activation field." Merz developed this relationship through direct observation of domain wall morphology changes via optical stress birefringence that arises at domain walls between pulsed DC measurements of switching current vs. time in barium titanate single crystals. These early forays allowed average values for switching velocity to be found over Merz's measurement timeframe and insufficiently describe the differences he observed between sideways domain growth in-plane with the sample and forward domain growth through the sample thickness. Inquiries into

the underlying physics of Merz's Law led to the development of a velocity model based on classical nucleation theory,[18] yet there remains a large disparity between the experimental observations and theoretical calculations of the activation field by an order of magnitude.[15–17] In an effort to account for this disparity, Miller and Weinreich[18] suggested that a series of nucleation events that occur along parent domain walls are responsible for the propagation of a domain wall and that switching velocity is then controlled by nucleation rate. This theory requires the existence of a sufficient number of nucleation centers in ferroelectric samples, but without quantifiable defect populations and sufficient understanding of their ability to lower the energy barrier to nucleation, this series of assumptions cannot sufficiently explain the Miller and Weinreich model.

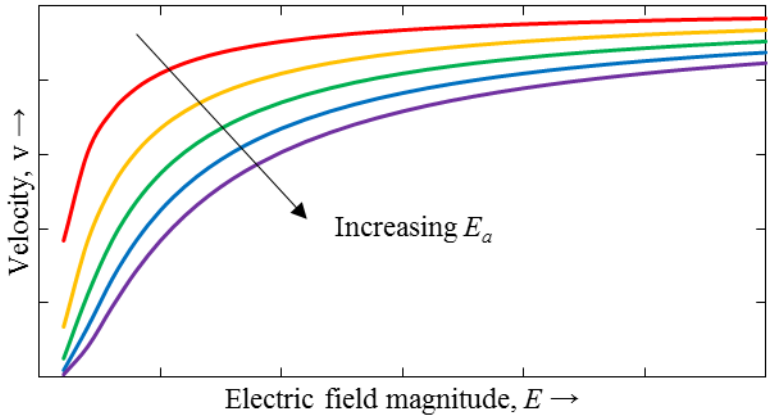

Figure 1.4: A graphical representation of Merz's Law, showing that as the activation electric field increases for a given system, the applied electric field must increase significantly for domain wall velocity values to rise to comparable levels.

Recent advances in characterization techniques, like the advent of piezoresponse force microscopy or *in situ* switching of FEs during transmission electron microscopy and x-ray diffraction,[8,19–21] have greatly assisted in collecting information on structure and polarization evolution during switching, yet each technique possesses complicating factors that present challenges when attempting to determine a true value and associated distribution for domain wall velocity, such as: changes in the magnitude of local electric fields, the varied characteristic switching times and fields between chemistries or even among different samples of the same nominal chemistry, and unknown quantities and magnitudes of energy barriers to polarization reversal.[4,22,23] The studies and techniques that are discussed in the remainder of this section

provide a summation of the recent attempts to address these complicating factors through both macroscopic and microscopic measurements of switching.

Macroscopic measurements of switching through application of high energy diffraction techniques have been used to observe stress evolution in polycrystalline ceramic bodies that contain high fractions of ferroelastic, non-180° domain walls.[21,24–31] An example of one such ferroelastic transition is schematically described in Figure 1.5 after Daniels *et al.*,[21] wherein a tetragonal ferroelectric undergoes two intermediate 90° switching processes before full polarization reorientation is achieved. Similar techniques have been used to investigate global 180° wall motion and domain densities, although the presence of intermediate switching stages present during switching in materials that are not crystallographically limited to polar and antipolar directions makes adapting diffraction techniques to less ferroelastic systems more difficult,[32–35] while stress evolution in materials that do possess only polar and antipolar vectors (such as $LiTaO_3$ and $LiNbO_3$) cannot be resolved directly via x-ray scattering due to time reversal symmetry making domain polarization direction impossible to distinguish. In addition, while these techniques are useful from the global perspective, they have difficulty resolving individual contributions from domain nucleation and domain growth.

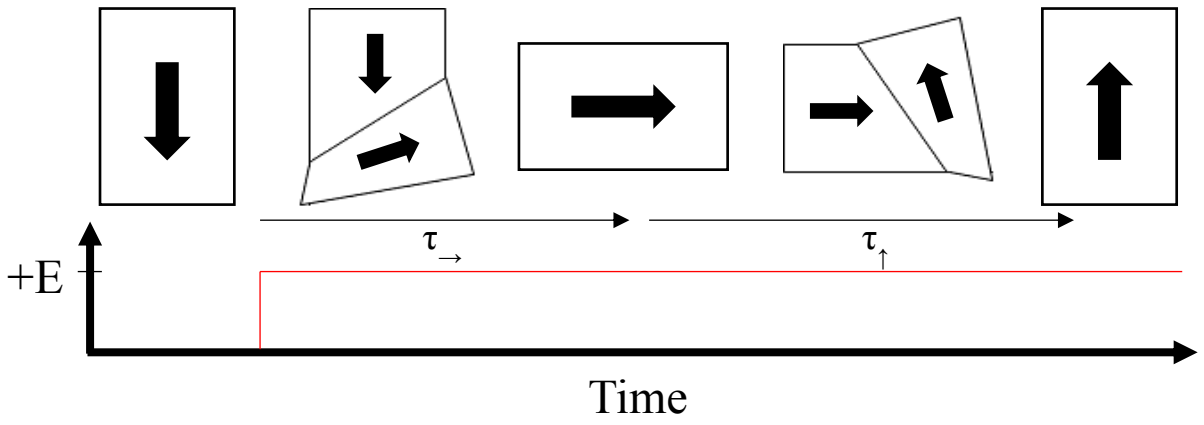

Figure 1.5: Schematic representation of polarization reversal. An out of plane variant (i.e., up or down) and an in-plane variant (i.e., a right arrow) demonstrate two successive 90° switching processes ($\tau_{\rightarrow}$ or $\tau_{\uparrow}$) in response to a step change in applied electric field.

Direct measurements of ferroelectric response through polarization vs electric field (PE) loops can help to distinguish between nucleation and growth by quantifying Barkhausen pulses (also known as Barkhausen noise or Barkhausen jumps). Barkhausen pulses are characterized by sudden spikes in transient current during polarization reversal as domain walls are depinned and travel rapidly through the microstructure until arresting once again at an energy barrier that cannot be overcome by the magnitude of the applied electric field.[36–38] Even this technique cannot fully resolve contributions to polarization switching between domain pinning and growth, however, as it has been shown that when growing domains merge or a nucleation event occurs rapdily, a sudden increase of polarization can also be measured, resulting in similar spikes in transient current signals.[39–41]

Quantification of pinning processes can be attempted through application of coercive and subcoercive methodologies. The Preisach model of hysteresis is applied to ferroelectricity to describe reversible and irreversible polarization processes at electric field magnitudes sufficient to reorient polarization vectors (coercive).[42,43] Preisach analysis differentiates between the two by utilizing first order reversal curve (FORC) testing to measure a bidimensional distribution of polarization values as a function of coercive field. The degree of symmetry in the distribution of forward-poling and reverse-poling coercive fields establishes the reversible and irreversible contributions to the poling process.[12,44–46]

Rayleigh analysis is complementary to Preisach measurements and is performed at sub-coercive electric field magnitudes.[47,48] By measuring dielectric permittivities as a function of escalating subcoercive AC electric fields, the intrinsic atomic lattice contributions to permittivity can be separated from extrinsic contributions originating from domain wall motion (Figure 1.6, after Schenk *et al.*[48]). Once field strength is sufficient to push domain walls beyond energy barriers, the irreversible polarization change is registered as a dielectrically lossy signal that increases permittivity. Plotting permittivity as a function of field strength yields coefficients that can reveal the ratio of reversible to irreversible processes.[12,27,49,50] Unfortunately, these methodologies require certain statistical assumptions (randomly distributed pinning centers of

unknown strength, for example) that preclude the assignment of quantifiable energy barriers to any individual defect.

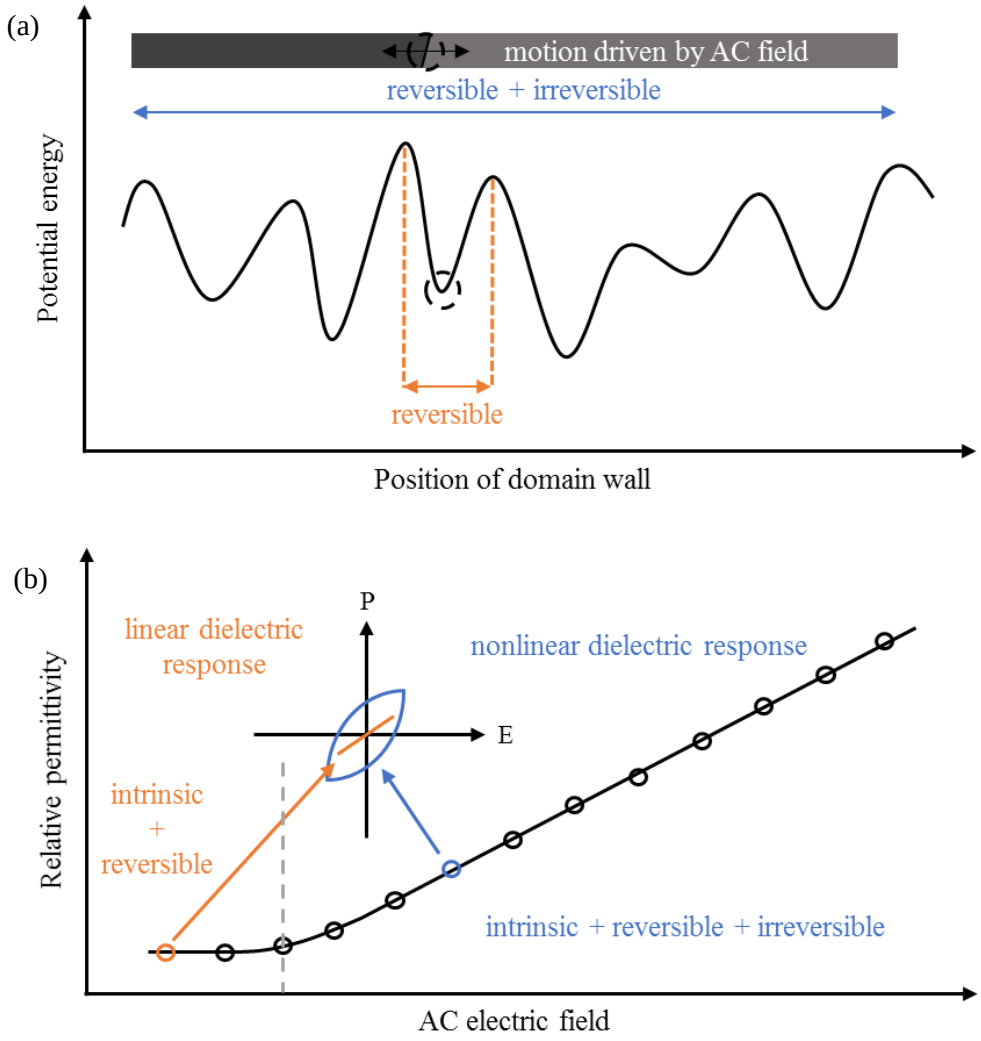

Figure 1.6: A simplified sketch of the underlying theory and characterization of Rayleigh behavior in ferroelectrics. (a) Position of a domain wall subject to an AC electric field in a random energy landscape. (b) Under small electric fields, intrinsic and reversible contributions to permittivity are measurable. Once irreversible energy barriers are overcome by a sufficiently large field, domain wall movement contributes to permittivity as well.

Nominally, direct observation of a single propagating domain wall as it encounters a defect presents a straightforward pathway to answering these existential questions regarding pinning. By utilizing a series of optically-active dopants, studies by Dierolf and coworkers designed to witness extrinsic defect-domain wall interactions in lithium niobate and lithium tantalate revealed that defect dipoles can be influenced tens

of microns away from the dopant ions.[51–58] The role of intrinsic point defect populations on coercive field magnitude differences between $LiTaO_3$ and $LiNbO_3$ crystals that possess a congruent chemistry which is 1.5 mol% lithium deficient vs. more stoichiometric crystals that are ostensibly free of intrinsic point defects was extensively investigated by Gopalan and associates.[59–66]

Given the variety of difficulties that are associated with direct measurement of domain wall velocity, measurements of separate – but related – properties may serve to provide inferential information regarding domain wall speeds. In establishing Merz's Law, Merz himself first noted a relationship between the maximum observed domain wall velocity in barium titanate and the acoustic velocity of the material: namely that the speed of sound was approached but never surpassed by the velocity of domain growth.[4] There have since been exceptions noted for this observation under very specific conditions,[67] but monitoring of acoustic phonon behavior through acoustic velocity and thermal conductivity measurements represents an opportunity to measure a ceiling of potential domain wall velocities that are less intrinsically limited by measurement parameters.

There have been many studies performed and many techniques developed to attempt to expose the role that material defects of all scales and types can play in the ferroelectric switching process. To robustly link this information from the single-dopant/single-domain wall level of investigation to the macroscale switching behavior and attempt to address the overarching question of "under what conditions do specific crystallographic defects act as either domain nucleation or domain wall pinning sites?" a material system needs to be selected that allows for a simplification of domain response and precise control of defect type. The lithium tantalate material system provides an opportunity for linking micro and macroscale ferroelectric responses to defect types. There exists ample work defining its intrinsic point defect species and acceptance of dopant ions in single crystal form, and producing polycrystalline specimens with a controlled microstructural orientation is conceptually possible. In addition, crystallography limits polarization reversal to 180° domain reorientation. Development and characterization of $LiTaO_3$ sample sets that can accomplish

the goal of providing a simplified ferroelectric system with finely controlled defect populations of a range of types is the focus of this thesis.

1.2 Lithium Tantalate

Lithium tantalate (LT) and lithium niobate (LN) are prototype uniaxial ferroelectrics that possess *R3c* crystal symmetry and are composed of stacked oxygen octahedra. These octahedra share close packed planes and are filled along the *c*-axis in sequences of the following pattern: … Li – Ta/Nb – □ – Li – Ta/Nb – □ … where the empty boxes represent unoccupied octahedra. Two formula units are required to describe the entire unit cells of these systems such that the position of staggered oxygens can be accounted for by two *c* glide operations. Above the Curie temperature, these materials adopt an inversion center ($3m \rightarrow \bar{3}m$), the Ta/Nb ions move to the center of their octahedra along the *c*-axis, and lithium ions move to the adjacent unoccupied octahedra through the intermediate oxygen plane. The direction of the cation offset below T_C defines the polarization vector of these materials.

$LiTaO_3$ and $LiNbO_3$ are commercially produced as single crystals grown from a melt through the Czochralski technique. These crystals are used in a variety of nonlinear optical applications and surface acoustic wave devices. To avoid cooling through phase fields where phase separation would occur, single crystal boules are produced at the congruently melting composition as opposed to the stoichiometric chemistry, as designated in Figure 1.7 below. This results in boules that are approximately 1.5 mol% Li_2O deficient. The exact compensation mechanism for this lithium deficiency has been heavily debated in the literature (and is summarized in Chapter 1.3), but the effect on multiple material properties – including Curie temperature, coercive field, refractive index, thermal conductivity, and more – is pronounced.

Although the work in this thesis was entirely performed on $LiTaO_3$, this document includes multiple instances where studies on the very similar and more commonly-studied LN are referenced. This practice is common throughout the literature; niobium and tantalum have identical ionic radii, the oxides have

isomorphic atomic structures, and many of the structural and functional characteristics of LN and LT are completely analogous with differences only in magnitude or applicable temperature range.

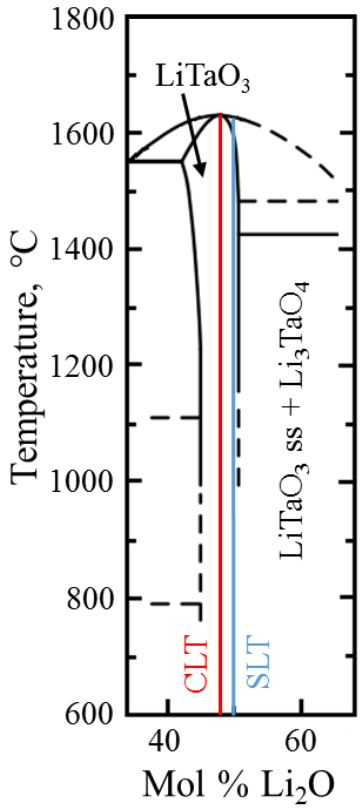

Figure 1.7: Modified Li_2O – Ta_2O_5 phase diagram from Martel, *et al*. (1981). Congruent (CLT) and stoichiometric (SLT) compositions of $LiTaO_3$ are denoted with red and blue lines, respectively. Reprinted with permission from American Ceramic Society Bulletin.

1.2.1 Compensation Mechanisms for Li_2O-deficiency

Three models have been discussed most commonly for defect compensation of the off-stoichiometry in congruent LT: $2V_{Li}' + V_O^{\cdot\cdot}$, $5Ta_{Li}^{\cdot\cdot\cdot\cdot} + 4V_{Ta}''''$, and $4V_{Li}' + Ta_{Li}^{\cdot\cdot\cdot\cdot}$, which will be referred to as the oxygen vacancy model, tantalum vacancy model, and the lithium vacancy model, respectively. Examining the structure of congruent LT reveals that the density of $LiTaO_3$ actually increases as lithium content decreases,[68–73] which, along with computer models that predict a low likelihood of development of $V_O^{\cdot\cdot}$,[74] leads to an assumption that this density increase is the result of $Ta_{Li}^{\cdot\cdot\cdot\cdot}$ defects that are compensated by V_{Ta}''''. Tantalum ions in six-fold coordination possess an ionic radius of 0.64 Å, which is smaller than that of lithium at 0.76 Å,[75] indicating that tantalum should be able to occupy lithium sites in the $LiTaO_3$

lattice, and increasing the fraction of tantalum-centered octahedra clearly increases the density of the material. The tantalum (niobium) vacancy model was examined through atomistic modeling in lithium niobate.[76] Donnerberg, *et al.* showed that the formation of a niobium vacancy is much less energetically favorable than that of a lithium vacancy when compensating a niobium antisite defect.[76] In addition, x-ray and neutron diffraction studies have lent credence to the lithium vacancy defect model.[71,73] Others then proposed that a combination of the tantalum vacancy and lithium vacancy models could be reconciled if the two defect schemes stacked in an ilmenite-type fashion with alternating cation sequences (…Li – Nb – □ – Nb – Li – □ – Li – Nb – □…) as opposed to the standard cation stacking sequence (…Li – Nb – □ – Li – Nb – □ – Li – Nb – □…).[77] This possibility was investigated via NMR spectroscopy by Ivanova, *et al.*[78] and Yatsenko, *et al.*,[79] who found that only the lithium vacancy model could account for the temperature dependence of NMR ^{7}Li spectra and that $Ta_{Li}^{\bullet\bullet\bullet\bullet}$ is likely surrounded by four V_{Li}'. The lithium vacancy model and resulting defect complex was further supported by x-ray and neutron diffuse scattering in congruent $LiNbO_3$ by Zhdanov, *et al.*,[80] Ivanov, *et al.*,[81] and Zotov, *et al.*[82] Despite this evidence, some debate has continued on the role of cation off-stoichiometry in the defect structure of $LiTaO_3$,[83–85] although most of the community agrees that the lithium vacancy model is the most likely intrinsic defect scheme to exist in the $LiTaO_3$ and $LiNbO_3$ systems.[38,66,86]

1.2.2 Confirmation of point defect scheme via DFT

Computational verification of several potential atomic defect schemes was investigated through density function theory (DFT) experiments by collaborators Dr. Prashun Gorai and Dr. Vladan Stevanovic at Mines. The regions of $LiTaO_3$ phase stability were investigated for a range of chemical potentials encompassing the congruent and stoichiometric chemistries, as well as a midpoint between the two, at 1300 °C, which is representative of potential sintering temperatures for the system, under both oxygen rich (pO_2 = 1 atm) and oxygen poor ($pO_2 = 10^{-15}$ atm) conditions. Dominant point defect pairs were assessed by determining the combination that had the lowest enthalpies of formation and normalized to the Fermi energy. The following defects were considered: V_{Li}', $Ta_{Li}^{\bullet\bullet\bullet\bullet}$, V_{Ta}'''''', Li_{Ta}'''', and $V_O^{\bullet\bullet}$.

The enthalpy of formation profiles from the DFT work are shown in Figure 1.8. The intersection of lines between two oppositely charged defects indicates how energetically favorable that particular defectcombination is to form. For each condition examined, the intersection of the lines associated with V_{Li}' and $Ta_{Li}^{\bullet\bullet\bullet\bullet}$ occurs at the lowest enthalpy of formation, meaning that these defects should be the dominant pair regardless of crystal chemistry and relative partial pressure of oxygen. Similar conclusions are reached via DFT and hybrid DFT calculations on the $LiNbO_3$ system.[85,87]

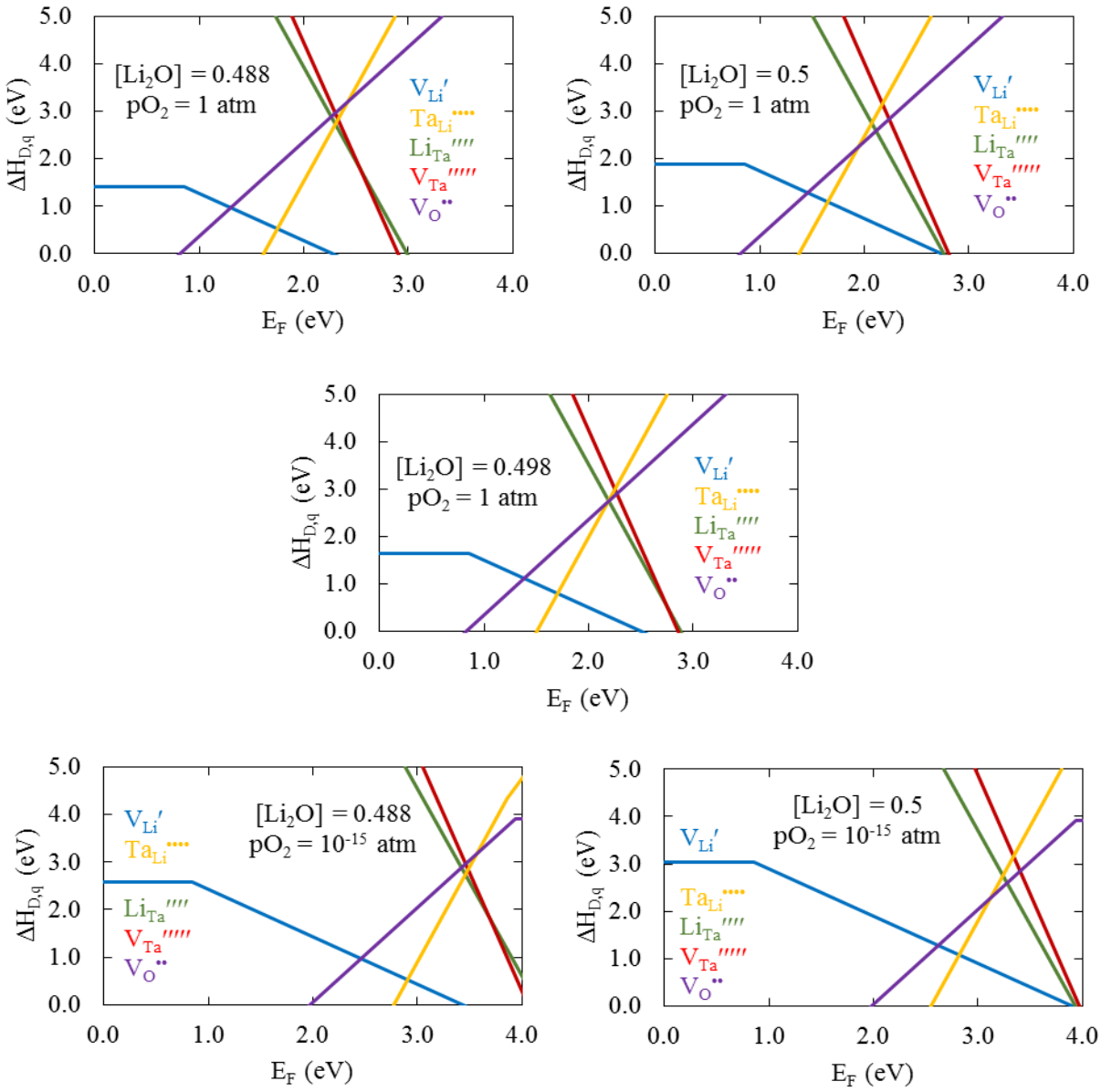

Figure 1.8: Enthalpies of formation for potential point defects in $LiTaO_3$ as a function of optimized Fermi energy for reducing and oxidizing conditions at three different Li_2O concentrations.

Estimations for the concentrations of the dominant point defects were also made at 1300 °C and are listed in Table 1.1. The total number of cation sites was found to be 1.82 x 10^{22} cm^{-3}. The number of point defects increases by multiple orders of magnitude as the chemistry of $LiTaO_3$ changes from the stoichiometric Li_2O concentration to the congruent one and varies minimally between relative pO_2 for a given composition.

Table 1.1: Estimated point defect concentrations as a function of $LiTaO_3$ composition and oxygen partial pressure.

[Li_2O], mol%	pO_2 (atm)	[V_{Li}'] (cm^{-3})	[$Ta_{Li}^{\bullet\bullet\bullet\bullet}$] ($cm^{-3}$)
50.0	1	7.51 x 10^{18}	3.69 x 10^{18}
50.0	10^{-15}	7.37 x 10^{18}	3.63 x 10^{18}
49.8	1	5.74 x 10^{19}	2.86 x 10^{19}
44.8	1	4.35 x 10^{20}	2.18 x 10^{20}
44.8	10^{-15}	4.20 x 10^{20}	2.10 x 10^{20}

1.2.3 Measurement of intrinsic defect concentrations via indirect methods

With the understanding that point defect populations are directly related to lithium deficiency in $LiTaO_3$ crystals, close monitoring of lithium concentrations is of primary interest. Chemical quantification of lithium by commonly accessible x-ray detection methods is frequently difficult or impossible because of the element's low x-ray cross section, rendering x-ray fluorescence and x-ray energy dispersive spectroscopy insufficient for this task. Nuclear magnetic resonance has been used to directly quantify Li concentrations in $LiNbO_3$ by Carruthers and Peterson, *et al.*[88,89] These studies were used to correlate the composition of LN single crystals to their Curie temperature, indicating a linear relationship between the two, where the congruent composition of LN, at ~ 1.5 mol% Li deficiency, possesses a $T_C \approx 1138$ °C and stoichiometric LN has a $T_C \approx 1198$ °C.[90] A similar linear relationship was observed between lithium content and Curie temperature in LT, where T_C of CLT is approximately 601 °C and T_C of SLT is approximately 701 °C.[63,91] Establishing the relationship between Curie temperature and chemical composition in these materials led to further links between material properties and chemistry, i.e., intrinsic defect populations, including: coercive field,[92–94] UV absorption edge,[61,95] optical damage threshold,[66,96] thermal conductivity,[97–99] and Raman vibrational spectra.[100]

Of particular interest in this thesis are the changes in vibrational modes in $LiTaO_3$ as point defect concentrations increase. At optical frequencies, Raman active modes increase in bandwidth from the increased disorder induced in the lattice and new, previously unassigned modes develop from the ilmenite stacking sequence that develops when lithium vacancy concentrations rise.[101–104] In fact, it has been shown previously that the intensity of the spurious modes in $LiTaO_3$ increases as the fraction of ilmenite-like defects likewise increases when lithium content decreases from the stoichiometric value.[105] Measurement of Raman spectra have been used in the above studies as an indirect quantification method of lithium concentration.

1.2.4 Controlling defect populations in the literature

The intrinsic point defect populations in $LiTaO_3$ have a large effect on several material properties, as expanded upon in Table 1.2 below. Given this fact, a thorough understanding of processes that control defect populations is of vital interest. As mentioned earlier in section 1.2, lithium tantalate single crystals are grown from a melt for commercial applications by the Czochralski technique at the congruent composition which is ~ 1.5 mol % Li_2O deficient. Varying the melt composition into the lithium-oxide-rich regime has been shown to produce crystals that are closer to the stoichiometric composition.[106] Application of a double-crucible method to the Czochralski technique to help control lithium oxide volatilization during crystal growth in conjunction with a significant excess of Li_2O of eight or nine mole percent has been shown to produce $LiTaO_3$ crystals with a final [Li_2O] = 49.9 mol%, as verified by Curie temperature measurements.[107]

Table 1.2: A selection of material property changes as a function of cation stoichiometry in $LiTaO_3$.

	Congruent LT	Stoichiometric LT
[Li_2O]	~ 48.5 mol%	50.0 mol%
Curie Temperature	~ 601 °C [63]	~ 701 °C [91]
Coercive Field	210 kV/cm [59]	1 kV/cm [93]
Thermal Conductivity	2.4 W/mK [183]	4.8 W/mK [183]

A thermal processing technique known as vapor transport equilibration (VTE) has been used to modify chemistry of $LiTaO_3$ single crystals after their growth to any point within the $LiTaO_3$ solid solution range of compositions. Most typically, a congruent crystal is placed in a loosely enclosed system above a powder source of lithium oxide vapor with the intention of increasing the lithium content closer to that of the stoichiometric composition. In this case, Li_2O is evolved from a two-phase mixture of $LiTaO_3$+Li_3TaO_4 through thermal decomposition of the Li_3TaO_4 phase that self-terminates because the two-phase powder is in equilibrium with the single crystals that are adsorbing the Li_2O vapor.[63,108] The VTE process conventionally occurs at temperatures in excess of 1200 °C and can require up to several hundred hours of treatment to fully lithiate a crystal, depending on its thickness.[97,109]

Despite the interest in control of Li:Ta stoichiometry via VTE over the last thirty years, the author could find only one quantitative report of Li diffusion in $LiTaO_3$ that takes place at a relevant temperature range for VTE,[110] meaning there is little understanding in the literature of the intermediate stages of this stoichiometry modification technique. This presents a problem for those seeking to fine-tune the VTE process and tightly control the intrinsic defect concentration in $LiTaO_3$.

Dopants of several species have been added to $LiTaO_3$ and $LiNbO_3$ melts in an effort to alter ferroelectric and optical material properties, including Curie temperature and optical damage thresholds.[96,111–117] These experiments and a selection of computational studies,[118,119] provide some knowledge of the solubility of various dopants and where they sit within the host lattices. Most dopants occupy vacant lithium sites in sub-stoichiometric $LiNbO_3$ and $LiTaO_3$. The most common of these is magnesium oxide, which has a high solubility in both lithium-based oxides. As MgO doping concentrations increase to a maximum of eight mole percent,[114] Curie temperatures increase to near-stoichiometric levels and optical damage is consistently reduced.[114,120] That these property changes trend in the same direction with increasing MgO concentrations as they do with Li_2O concentrations that increase toward the stoichiometric value from the congruent one indicates that filling lithium vacancies with non-native ions can also lower the overall energy of the lattice.

1.2.5 Polycrystalline Lithium Tantalate

Polycrystalline $LiTaO_3$ is not currently produced for any commercial applications, despite the usual driving forces of increased geometric, compositional, and cost benefits that are associated with polycrystal forming methods as opposed to single crystal growth. Two substantial barriers must be overcome to make fabrication of dense, polycrystalline LT a reality: a large disparity in ionic mobilities and a highly anisotropic coefficient of thermal expansion (CTE, $\alpha_a \approx 16 \times 10^{-6}/°C$, $\alpha_c \approx 4 \times 10^{-6}/°C$). Recent works, some of which the thesis author contributed to, explored methods of hot pressing and the development of grain boundary-pinning secondary phases to control microstructures and mitigate CTE-related stresses which result from dissimilar shrinkage rates along different crystal axes.[121–125] Although several of these studies achieved $LiTaO_3$-based specimens with ≥ 95 % relative theoretical densities, the methods used were not attractive for commercial production and tended to produce multi-phase samples with inferior dielectric quality. A process that yields single phase, dense, polycrystalline $LiTaO_3$ has yet to be reported.

1.3 Research Goals

Although there exists information regarding the removal of point defects in single crystal $LiTaO_3$, a fundamental understanding of the VTE process is lacking. Further studies are required to understand lithium diffusion in LT, which will in turn inform methods for controlling defect populations for densification and grain growth of polycrystalline $LiTaO_3$. Linking these pieces of information together should allow for a complete sample set to study the role of defects in ferroelectric $LiTaO_3$ properties.

The remainder of the thesis is devoted to addressing the following research goals:

1. Develop a more thorough understanding of the VTE process by determining diffusion coefficients for lithium in *z*-cut single crystal $LiTaO_3$ based on partial VTE anneals.
2. Understand the impact of point defect concentrations on thermal conductivity by extending studies across the entire solid solution chemistry range of congruent and stoichiometric $LiTaO_3$ single crystals.

3. Garner insight into the role of intrinsic point defect concentrations in densification and grain growth of polycrystalline $LiTaO_3$ by controlling atmospheric Li_2O to prevent lithium volatilization in sintered specimens.
4. Explore templated grain growth (TGG) as a viable methodology to texture polycrystalline $LiTaO_3$ to mitigate CTE-induced stresses.

1.4 Organization

The thesis chapters that follow present data from a selection of experiments that were designed to meet the research goals above. Chapter 2 details a suite of reduced-temperature VTE-like anneals that are used to establish lithium gradients, and associated point defect gradients, which are then measured via indirect chemical quantification to calculate lithium diffusion coefficients along the *c*-axis of $LiTaO_3$ single crystals. The insights gained during those studies were used to develop the sample set that is the focus of Chapter 3, wherein thermal conductivity measurements are performed on a set of $LiTaO_3$ samples that span the solid solution chemistry range from the congruent to stoichiometric compositions. Adapting the VTE technique to control lithium stoichiometry in polycrystalline $LiTaO_3$ is the focus of Chapter 4. The role of cation stoichiometry on grain growth is discussed there along with the possibility of mitigating CTE-induced stresses using templated grain growth. The results of Chapters 2 through 4 are summarized in Chapter 5 while Chapter 6 suggests future studies that could be done to build upon the work of this thesis.

CHAPTER TWO

LITHIUM DIFFUSION IN LITHIUM TANTALATE AS MEASURED BY CONFOCAL RAMAN SPECTROSCOPY

Intrinsic point defect populations that arise due to lithium deficiency are known to have profound effects on ferroelectric and other material properties of lithium tantalate. Although vapor transport equilibration has been shown to be an effective method of increasing lithium concentration in Li-deficient single crystals, little is understood about the intermediate stages of this process. In this chapter, a two-step approach to vapor transport equilibration is adapted to develop gradients in lithium concentration which in turn establishes a cation point defect gradient. Lithium diffusion coefficients are estimated through the measurement of Raman-active optical phonon mode intensities that are directly related to these point defect concentrations in $LiTaO_3$. These reports of Li diffusion coefficients are the first within this elevated temperature range since 1974. A subset of the work represented in this chapter was recently published in the Journal of Material Science under the title, "Lithium diffusion in lithium tantalate as measured by confocal Raman spectroscopy" and is authored by Jacob Ivy and Dr. Geoff Brennecka. The article can be found at doi: 10.1007/s10853-022-07105-y.

2.1 Vapor Transport Infiltration

Vapor transport equilibration has been explored for nearly thirty years to modify the chemistry of lithium tantalate and lithium niobate single crystals after their growth. Historically, reports that utilize this technique have produced samples that possessed a uniform composition that is dependent on the duration of the VTE treatment and the thickness of the crystals.[63,97,101,126,127] Samples exit vapor transport equilibration, which often includes multiple steps that take place at different temperatures, with a uniform composition, meaning that there is a gap in the understanding of the intermediate stages of this process. Interrupted VTE treatments and a novel method of tracking lithiation in $LiTaO_3$ are explored here to establish lithium diffusion coefficients at VTE-relevant temperatures to fill this knowledge gap.

A fundamental study of VTE-treated samples that are interrupted prior to full equilibration was pursued in this work. The thermal processing steps of these experiments are broadly referred to throughout the rest of this document as vapor transport infiltration (VTI) to distinguish the new experiments from prior multi-stage work that produced $LiTaO_3$ specimens with a uniform composition. The VTI anneals in this study utilized z-cut single crystals of congruent $LiTaO_3$, 10 x 10 x 0.5 mm, purchased from MTI Corp. Starting Curie temperatures were confirmed to be ~601 °C via temperature-dependent impedance measurements using painted silver electrodes and an HP 4294A impedance analyzer with 500 mV oscillator from 1 kHz – 1 MHz. These specimens were heated and cooled at a rate of 2 °C/min under ambient atmospheric conditions and a short circuit configuration. Only the cooling data are reported here.

The crystals were VTI treated in an enclosed platinum crucible and fully buried in a two-phase mixture of reacted powder originally comprising 40 mol% Li_2CO_3 and 60 mol% Ta_2O_5 as a lithium oxide vapor source, as shown schematically in Figure 2.1. The Pt crucible and contents were heated to temperatures between 950 and 1100 °C at a rate of 5 °C/min and soaked for between 15 and 30 hours. After cooling to room temperature at 2 °C/min, the crystals were sectioned; one half of each crystal was used directly for measurements, while the second half was placed back into a furnace for additional annealing in an ambient atmosphere without the presence of excess lithium oxide with the goal of equilibrating any chemical gradients that arose during VTI. These equilibration anneals varied in duration from 12 to 25 hours, but all took place at 1350 °C.

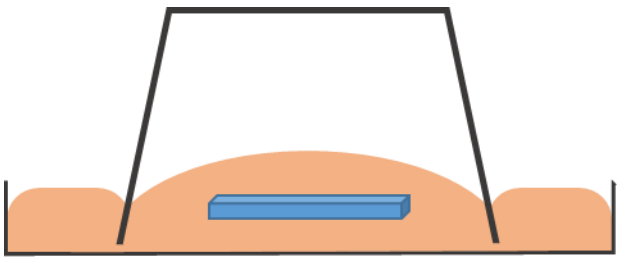

Figure 2.1: A schematic depicting setup for the initial stage of the VTI anneals, where the $LiTaO_3$ single crystal (blue) is buried in $LiTaO_3$ + Li_3TaO_4 powder (orange) and covered by a platinum crucible (grey) to help maintain a Li_2O overpressure.

2.2 Chemical Characterization Post VTI

As mentioned previously in Chapter 1.2.3, lithium concentrations are difficult to quantify via easily accessible x-ray fluorescence methods. Quantification of lithium chemistry in samples that were submitted to VTI treatments was pursued by indirect means. Measurement of a crystals Curie temperature allowed for quantifiable Li concentration of the entire crystal to be determined, while localized qualitative measurements of Li concentration were enabled through confocal Raman analysis.

2.2.1 Global Chemistry from Curie Temperature Measurements

Initial chemical information for VTI treated $LiTaO_3$ was obtained via temperature dependent permittivity measurements to determine the Curie point. The upper portion of Figure 2.2 gives the permittivity curves for the commercially produced CLT and SLT crystals. These peaks in permittivity that indicate T_C are sharp and centered near the temperatures that are well associated with their compositions.[57]

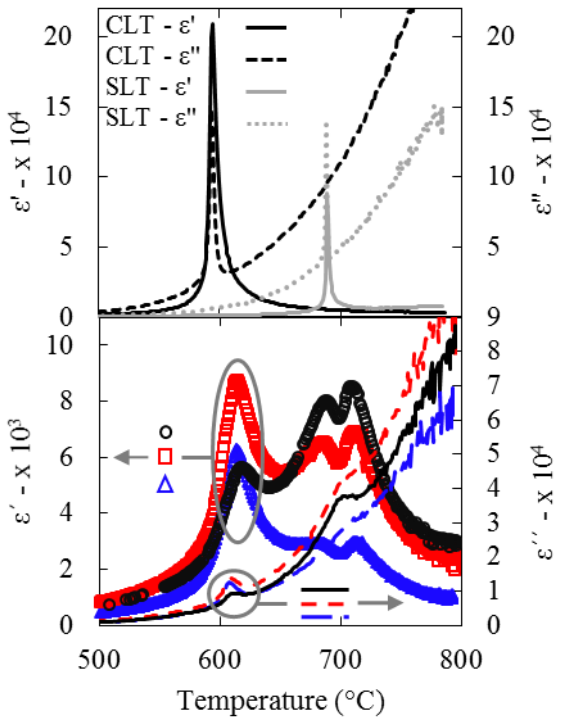

Figure 2.2: Curie temperature measurements for $LiTaO_3$. (Upper) Real and imaginary relative permittivity, ε´ and ε´´, respectively, of untreated CLT and commercially VTE annealed SLT. (Lower) Permittivities of specimens immediately after VTI treatment.

The lower portion of Figure 2.2 shows the effect of the low-temperature VTI anneals on the temperature-dependent permittivity of the originally-CLT specimens. In this figure, blue (triangles and dashed) lines represent a specimen that underwent VTI at 950 °C for 15 hours, red (squares and dotted) lines represent a specimen VTI treated at 1000 °C for 10 hours, and black (circles and solid) lines represent a specimen VTI treated at 1050 °C for 10 hours. Each sample that is shown in this figure exhibits two Curie temperature peaks, one at ~ 601 °C and the other at ~ 701 °C, which are the temperatures associated with congruent and stoichiometric $LiTaO_3$ as seen in the upper plot of Figure 2.2. This suggests that both SLT and CLT chemistries are present within these specimens after the VTI treatments, although there is no way to be certain which volumes of the specimens are dominating permittivity contributions at a particular temperature from these measurements alone. Additionally, the permittivity peaks of the VTI specimens are much broader than the peaks of the homogeneous commercial specimens whose homogeneous chemistries lie at the congruent and stoichiometric points. This is consistent with broad chemical gradients in the lab-treated specimens that spans these distinct stoichiometry regions. There is a general trend amongst these samples that the VTI anneals that took place at higher temperatures yield permittivity curves with a lower magnitude peak at the characteristic congruent temperature and a higher magnitude peak at the characteristic stoichiometric temperature. This suggests that a higher temperature VTI treatment produces a higher volume fraction of SLT but is neither quantitative nor conclusive from permittivity measurements alone.

2.2.2 Local Chemistry from TOF-SIMS

Direct quantification of chemical gradients in VTI treated $LiTaO_3$ crystals was sought through time-of-flight secondary ion mass spectroscopy (TOF-SIMS). Although this technique is most adept at detecting small amounts of impurity or dopant ions in a well-known matrix material, the relative difficulty of tracking lithium quantities with x-ray based detection methods warranted the attempted use of TOF-SIMS. The following material makes use of the TOF-SIMS system at the Colorado School of Mines, which was supported by the National Science Foundation under Grant No. 1726898.

A CLT reference and a selection of VTI single crystal specimens were mounted in crystal bond polymer in a cross sectional orientation and polished to a 1 µm finish. Ion profiles were collected in a static configuration as opposed to depth profiling along the *c*-axis of the specimens to mitigate specimen charging issues as well as to reduce measurement time, as the area of interest was quite large at ~ 500 x 500 µm since the cross-sectional thickness of the crystals was 500 µm. A primary ion source of bismuth at 30 keV in a randomized raster mode was used for these studies.

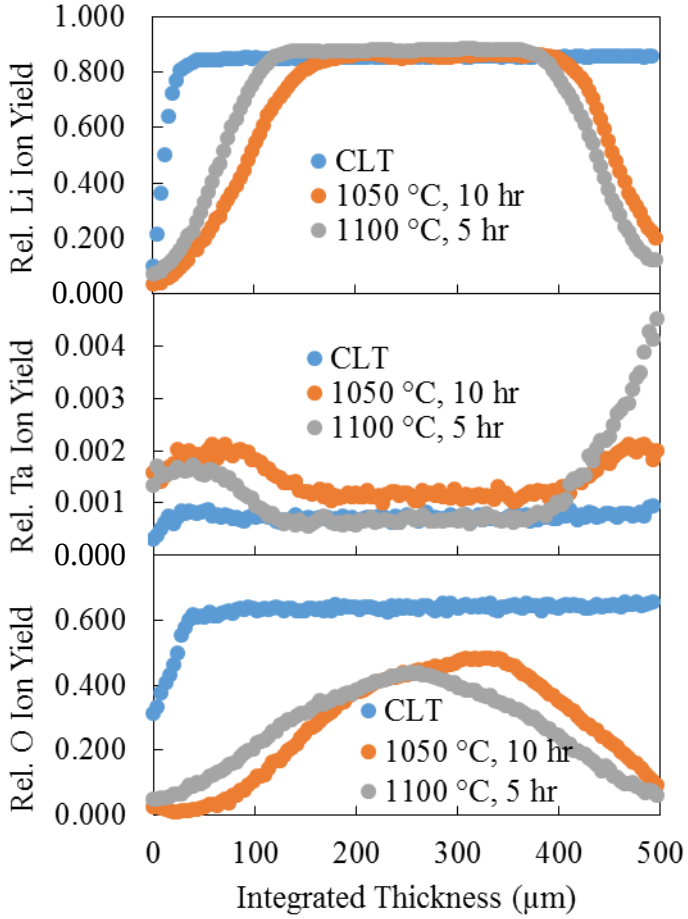

Figure 2.3: Normalized ion yield for congruent and VTI annealed $LiTaO_3$ single crystals. Integrated thickness values of 0 and 500 µm represent surfaces of the *z*-cut specimens. According to these TOF-SIMS profiles, VTI treated specimens exhibit lithium and oxygen deficiencies at their surface and tantalum enrichment which is counter to expectation.

The ion profiles that were reported from the TOF-SIMS analysis are shown in Figure 2.3 above. Each ionic species was relativized to the total cation or anion counts, as appropriate, for the specimen to

which each profile belonged. These data appear to indicate that the VTI process leaves lithium and oxygen deficient and tantalum rich regions at the surface of the treated specimens, as compared to the untreated CLT. Such profiles are inconsistent with diffusion of lithium from the surrounding environment into the crystals. A constant overpressure of Li_2O vapor whose magnitude is based on the temperature of VTI or VTE treatment acts as a constant source of lithium to be exchanged with the initially lithium-deficient single crystals. Lithium loss from the annealed specimens would be highly unlikely, and impedance data used to track T_C for these specimens shows similar profiles to those in Figure 2.2, wherein lithium pickup is evidenced by a permittivity peak near ~701 °C. Topography and sample orientation were also controlled for these samples and is not believed to play a role in the data profiles shown here. Because the TOF-SIMS data are not consistent with either fundamental diffusion kinetics or macroscopic tests of properties known to correlate with Li stoichiometry, an alternative technique for characterization of lithium content in these samples is needed.

2.2.3 Local Chemistry from Confocal Raman Analysis

Raman analysis presents an opportunity to study lithiation as a function of depth and VTI parameters in lithium tantalate. Raman spectra, as mentioned in Chapter 1.2.3, are tied directly to point defect concentrations in this material. Increasing concentrations of lithium vacancy and tantalum antisite defect complexes give rise to peak broadening in some Raman bands due to the increased structural disorder as well as the development of additional bands attributed to the increased fraction of ilmenite-type octahedra stacking that differs from the native oxygen octahedra stacking pattern.[101,102,104,105] Employing a confocal methodology to measure Raman spectra in VTI-treated $LiTaO_3$ provides sufficient spatial resolution to measure an optically active vibrational spectrum from a specific volume of material. This technique is uniquely applicable to transparent single crystals, as scattering events at grain boundaries in polycrystalline materials would quickly limit the depth of penetration for the light source.

Confocal Raman spectroscopy was performed using a WiTec alpha300 R instrument outfitted with a 532 nm incident laser in $Z(XY)\bar{Z}$ backscatter configuration to estimate the stoichiometry profile through

the bulk of VTI annealed lithium tantalate single crystals. This was accomplished by changing the focal depth of the sampling plane in 5 µm steps, collecting and summing ten individual Raman spectra, and monitoring the evolution of vibrational bands attributed to the intrinsic point defect complexes of the material, schematically shown in Figure 2.4. An incomplete compilation of Raman data is given in Figure 2.5 to provide a visual representation of the changes evident in the spectra as a function of measurement depth into a VTI treated specimen. Each spectrum was normalized to the intensity of the A_1(LO4) mode at ~862 cm^{-1} before being plotted because this mode is both highly intense and should receive little to no contribution from lithium or tantalum motion.[128,129] Several changes are noticeable in the spectra shown in Fig. 2.5 but most notable is the evolution of the band near 745 cm^{-1}. This band provides an optimal source of monitoring point defect concentrations and, by extension, lithium concentration as a function of depth and VTI parameters because it is distinct from other vibrational bands and has been attributed to point defect populations by prior works.[101,105,130]

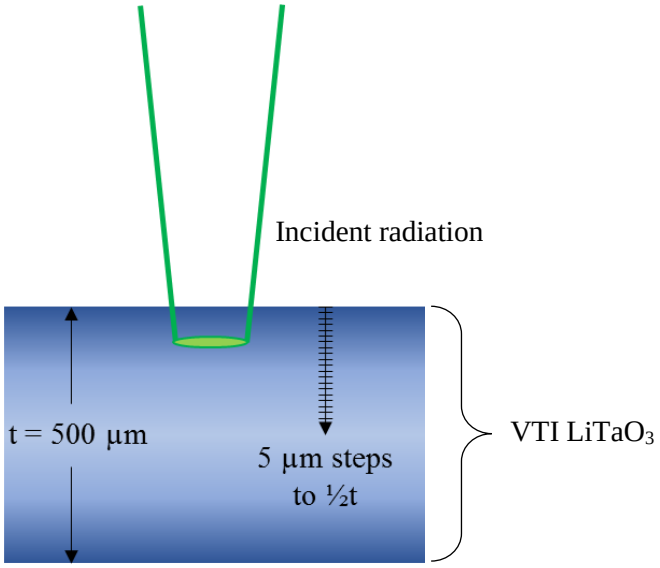

Figure 2.4: A schematic representation of the confocal Raman spectroscopy performed in this work. A VTI treated *z*-cut $LiTaO_3$ single crystal is shown with an unknown lithium vacancy gradient indicated by the change in shading. The confocal Raman focal plane, $\lambda = 532$ nm, is lowered through the ½ of the thickness of the crystal, collecting vibrational spectra in 5 µm increments.

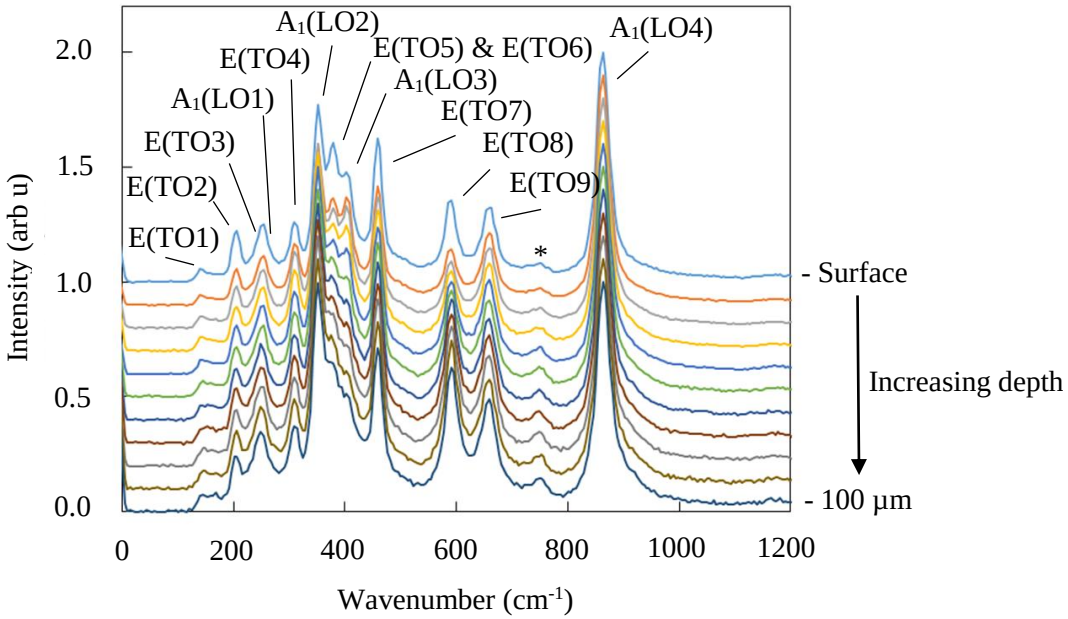

Figure 2.5: Confocal Raman data from a depth profile down the *c*-axis of a VTE treated $LiTaO_3$ crystal. Half of the collected scans from the complete depth profile are shown to prevent data crowding, in addition to shifting the data vertically for clarity. The known Stokes modes are labelled above, and one of the primary extraneous modes that develop with the presence of intrinsic point defects is highlighted by the asterisk. Very little change is observed beyond 100 µm to the marked defect mode, indicating that lithiation has not proceeded beyond this depth. Further scans are not shown here.

To better visualize the changes in the 745 cm^{-1} mode, the maximum intensity is normalized to the intensity of the A_1(LO4) mode in a series of Raman spectra and then plotted as a function of depth for a variety of VTI treatment conditions. Several of these data are plotted in Figure 2.6 for probe depths of up to 200 µm, beyond which the signal to noise ratio decreased rapidly and little to no change in the intensity of the defect-associated Raman band is observed. Both plots in Figure 2.6 contain compilations of intensity ratio data of the two targeted Raman peaks for samples that underwent VTI at varying times and temperatures, the specifics of which are given in the figure caption. In both plots the signal ratio is lowest at the surface of the samples, indicating a decrease in lithium content from the surface of the sample into the bulk. While this measurement does not directly quantify Li content, it has been shown previously that mass transport of Li in this system stops when the Li_2O concentration reaches 50.5 mol%.[97,131] For all samples that were VTI treated at a given temperature, an increase in VTI time appears to increase the lithium concentration at the surface as well as increase the thickness of the lithium rich surface layer, as expected

from classical applications of Fick's Laws.[132] This is demonstrated in the upper portion of Fig. 2.4 by a dataset from samples VTI treated at 950 °C. Increasing the temperature of the VTI treatment has a similar effect, reducing the defect peak intensity and increasing the depth of the lithiated surface layer as shown in the lower plot of Fig. 2.4. A Raman profile of a commercially VTE treated $LiTaO_3$ wafer (Crystal Technology, Inc., VTE parameters unknown, Li:Ta ~0:994) has been added to these plots to provide a reference for comparison to the in-house treated specimens and shows that even a nearly fully stoichiometric specimen retains measurable amounts of V_{Li}' and Ta_{Li}'''' defect complexes.

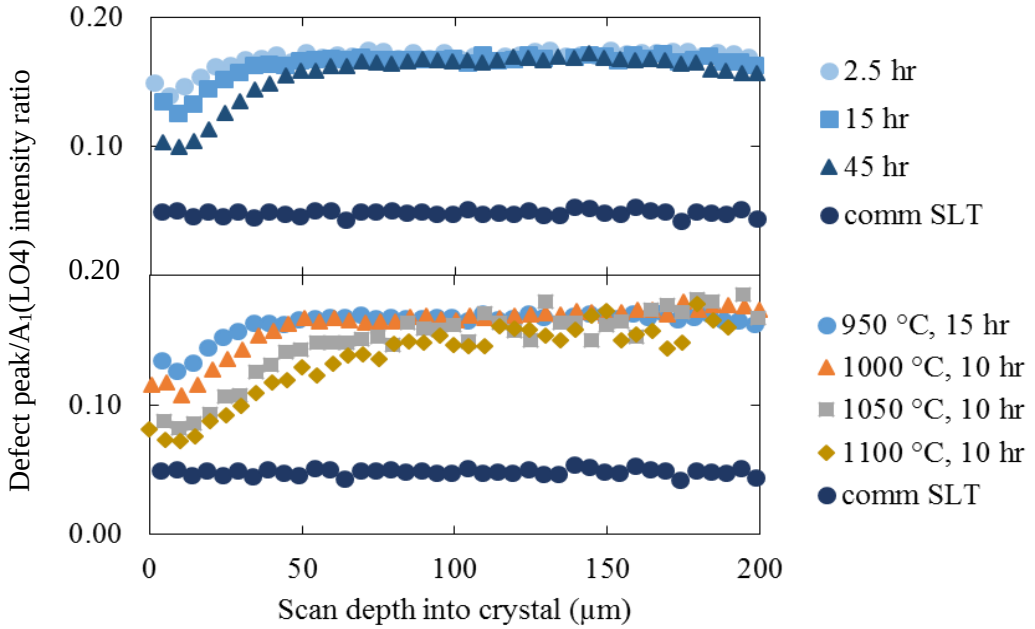

Figure 2.6: Intensity ratios for the Raman peak associated with intrinsic defect concentration vs. the A_1(LO4) mode plotted as a function of focal depth into VTI treated $LiTaO_3$ single crystals. (Upper) Signal vs depth profiles of different samples VTI treated at 950 °C for 2.5, 15, and 45 hours. (Lower) A comparison of many specimens VTI treated at different times and temperatures. Data from a commercial VTE treated stoichiometric crystal are shown for comparison to confirm that a nonzero signal is detectable in (nearly) fully lithiated $LiTaO_3$.

2.2.4 Equilibration of Chemical Gradients

Peaks in permittivity (indicative of T_C) sharpen considerably after the samples were annealed under ambient conditions and trend toward a single peak that is characteristic of the overall chemistry of the sample. The data in Figure 2.7, whose coloring and symbol scheme follows directly from the lower half of

Figure 2.2 to indicate the parameters for the initial stage of VTI, show the relative permittivity profiles from those selfsame samples after ambient atmosphere equilibration anneals at 1350 °C for 25 hours (blue triangles and dashed line), 12 hours (red squares and dotted line) and 12 hours (black circles and solid line). Cases such as those shown in the lower half of Figure 2.2, where the post-equilibration permittivity data have not yet converged to a single temperature, imply that additional annealing time is required to fully remove the chemical gradient within these samples. The ε′ data for the sample that was VTI annealed at 950 °C for 25 hours (blue triangles and dashed line) were multiplied by 10x in Figure 2.7 to better distinguish those curves from the other datasets. These data seem to indicate that the spread in lithium concentration within these samples that was the result of VTI treatment has been reduced, yet impedance spectroscopy alone cannot quantify the stoichiometry of these $LiTaO_3$ crystals post VTI or post equilibration annealing.

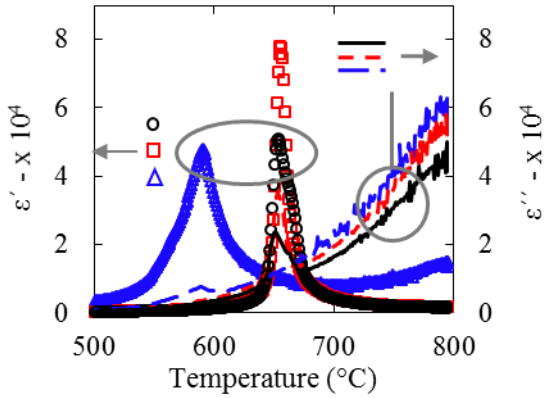

Figure 2.7: Real and imaginary permittivities for the same VTI-treated specimens from Fig. 2.2 after undergoing equilibration annealing at 1350 °C for 25 hours (blue triangles and dashed line), 12 hours (red squares and dotted line) and 12 hours (black circles and solid line).

Raman spectroscopy data were collected after secondary equilibration anneals to spatially resolve the cation stoichiometry of the specimens. The A_1(4LO)/defect peak intensity ratio data are shown in Figure 2.8 as a function of scan depth and are directly compared to the same data type for the post-VTI specimens. According to these data, the equilibration heat treatments provide sufficient energy to smooth the cation gradient and distribute the lithium that was built up in the surface of the VTI crystals, establishing a more uniform point defect population throughout the bulk of the specimens.

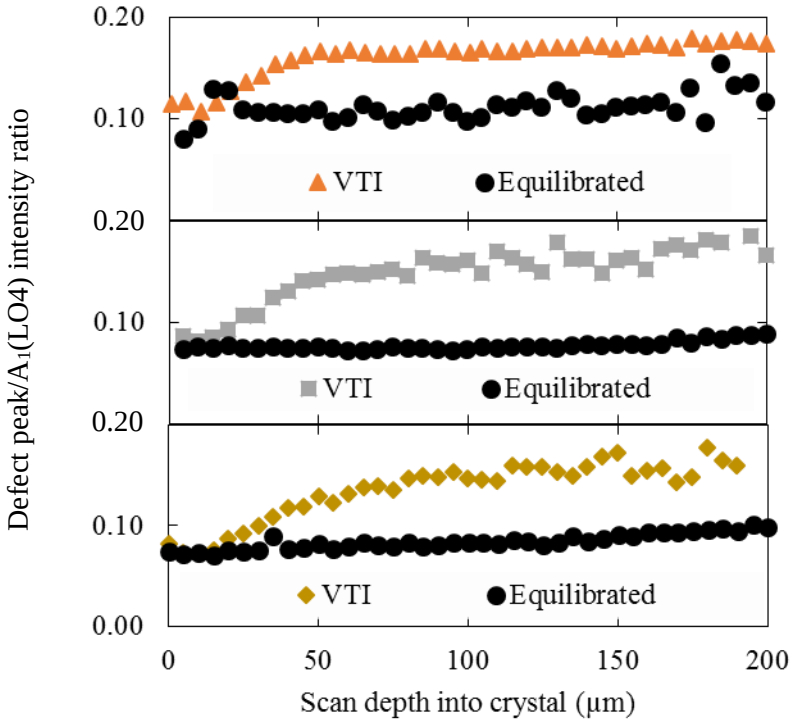

Figure 2.8: Comparisons between the VTI-treated samples from Fig. 2.6 (colored) and their counterparts after having undergone the equilibrium annealing process to homogenize crystal chemistry (black) for 12, 10 and 10 hours.

The two-step VTI processing explored in this work imparts lithium to the $LiTaO_3$ single crystals at lower temperatures than conventional VTE treatments, which may be important for VTE processing of thick CLT slabs. It has been reported by Yang *et al.*, that twin defects are prevalent in $LiTaO_3$ specimens between 1.0 and 3.2 mm thick when VTE processed at temperatures of 1200 °C and above.[133] Similar twinning defect development was observed in the 0.5 mm thick CLT crystals used in this work, although their concentrations and orientations were not investigated as this was deemed outside the scope of this work. Multiple authors noted that cracks form in the VTE-treated $LiTaO_3$ where twin interlayers intersected due to stress build-up from a combination of electrostatic and mechanical forces occurring within the intersecting twin bands.[133–135] Twin band and crack development was not observed in the VTI-treatments performed in this work, indicating that lowering the temperature of lithiation might provide an avenue to increase production yield of VTE-SLT.

2.3 Determination of Diffusion Coefficients

The partial lithium pickup from the VTI anneals established measurable point defect profiles that were mapped with confocal Raman spectroscopy. Reduction of the intrinsic point defect complexes of non-stoichiometric $LiTaO_3$ allowed the tracking of a lithium concentration profile and thus the determination of lithium diffusion coefficients from the Raman data. These coefficients were calculated by fitting a modified error function, given below, to the Raman profiles:

$$c(x,t) = A + Berf\left(\frac{x+y}{\sqrt{4Dt}}\right) \tag{2.1}$$

In this equation, *c(x,t)* is lithium concentration as a function of position in the sample and duration of VTE treatment, *A* and *B* are unitless constants, *D* is the diffusion coefficient, *t* is the duration of the VTE treatment, *x* is depth into the sample, and *y* is an offset factor to *x* that shifts the inflection point of the error function to the proper location within the relithiated surface layer to compensate for the potential of an increasing depth of a fully lithium-saturated region of $LiTaO_3$. The use of an error function to find diffusion coefficients provides a simple solution to Fick's second law, but it necessitates certain assumptions about the diffusion conditions, namely: that the system consists of two semi-infinite bodies, that diffusion is constant, and that in-diffusion of lithium is only occurring during the soak step of VTI and not on heating or cooling.

Diffusion studies in $LiNbO_3$ and LN/LT mixed materials have previously shown that there exists an orientation dependence to the diffusivity of lithium in these materials, wherein lithium diffusion is up to 72% faster along the *c*-axis than within the *ab* lattice plane, depending on composition and temperature.[136,137] A difference in diffusivity vs. orientation of this magnitude allows us to ignore possible in-plane contributions to lithiation in these diffusion coefficient calculations.

Locating the Matano plane through a Boltzmann-Matano analysis to ensure that the integrated areas bound by the diffusion profile are equal on both the surface and crystal-bulk sides of the concentration curve would be one method to increase the accuracy of the diffusion coefficients calculated here.

Additionally, full consideration of ambipolar diffusion principles to account for tantalum diffusion in concert with lithium would be prudent for a more complete discussion of multi-species diffusion in $LiTaO_3$. However, as the underlying goal of this work is primarily to fabricate samples for subsequent property studies, a more complex analysis is outside the scope of this thesis.

Equation 2.1 is not directly bound by any starting or final chemical information, so another calculation with a slightly more structured set of boundary conditions was utilized to confirm the coefficients indicated by this profile fitting method. Inserting the chemical information that can be gained from the known starting chemistry (congruent) and the final chemistry as determined by the Curie temperature after the VTI-treated $LiTaO_3$ crystals were subjected to equilibration anneals, as well as the depth at which the chemistry of the samples reaches the congruent composition from the Raman profiles, adjusts equation 2.1 to be written in the following form:

$$c(x,t) = c_i + (c_s - c_i)erfc\left(\frac{x+y}{\sqrt{4Dt}}\right) \tag{2.2}$$

where c_i represents the initial chemistry of the crystal, i.e., congruent, and c_s is the chemistry of the lithiated surface layer of the specimen as determined by the best fit of the Raman profile considering an upper limit of 50.5 mol% Li_2O due to the thermodynamic termination of any mass transfer during VTE and VTI. The resulting diffusion coefficients for lithium in $LiTaO_3$ are displayed in Figure 2.9. Reports for similar diffusion coefficients are available in the literature for lithium niobate but are largely lacking for lithium tantalate.

Manually applying the chemical boundary information into the error function equations does not appear to have significantly impacted the diffusion coefficients calculated in this work, as the coefficients differ by less than 3.5×10^{-10} cm^2/sec at all investigated temperatures adding confidence to the conclusions. The mean lithium diffusion coefficients found at 950 °C and 1100 °C are 4.2×10^{-11} cm^2/sec and 2.9×10^{-10} cm^2/sec, respectively. Data on lithium outdiffusion in $LiTaO_3$ as a function of temperature, from Carruthers *et. al.*,[110] remains within an order of magnitude of our data, suggesting that surface adsorption

and desorption reactions are not rate-limiting steps in lithium gain or loss during the VTI and VTE processes. Figure 2.9 also features lithium diffusion coefficients in $LiNbO_3$ for a visual reference.[110] All of the coefficients being reported for $LiTaO_3$ are noticeably lower than those for $LiNbO_3$, though this phenomenon is not unexpected given the relative proximity to the melting point.[138,139]

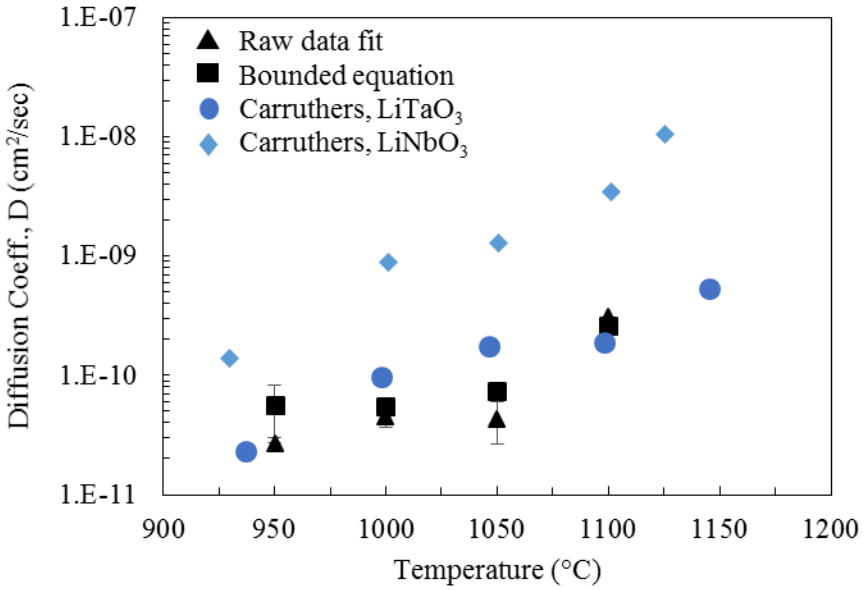

Figure 2.9: Diffusion coefficients for lithium in VTE treated $LiTaO_3$ calculated from Raman and Curie temperature data and compared to literature values for $LiTaO_3$ and $LiNbO_3$ along the polar axis.

2.4 Summary

Low temperature vapor transport infiltration was used to develop a lithium concentration gradient in lithium tantalate single crystals, which was later removed through a chemistry-equilibrating and stress-reducing anneal in ambient atmosphere. Lithium concentration profiles were inferred from confocal Raman spectroscopy measurements of point defect concentration, and diffusion coefficients of ~4.2 x 10^{-11} to ~2.9 x 10^{-10} cm^2/sec were calculated for lithium in $LiTaO_3$ between 950 and 1100 °C. Curie temperature values determined by permittivity measurements suggest that these conditions achieve a nearly-stoichiometric composition within the outer ~15 µm of the single crystals, and that, as vapor transport infiltration temperature increases, a lithium-enriched surface layer is formed between 30-80 µm deep into the crystal bulk before the cation ratio returns to that of the congruent composition.

CHAPTER THREE

IMPACT OF INTRINSIC DEFECT CONCENTRATIONS ON ACOUSTIC PHONON DYNAMICS IN LITHIUM TANTALATE

Expanding upon the work reported in Chapter 2, $LiTaO_3$ single crystals were VTE treated to establish specimens with an array of Li_2O concentrations which were then used in a series of experiments to examine the role of point defect populations on acoustic phonon behavior. The techniques used and discussed include inelastic neutron scattering, speed of sound measurements via ultrasonic transducers, and thermal conductivity measurements performed via two thermoreflectance methods. These data were collected in an attempt to validate the long-held theory that polarization switching speeds are limited by acoustic velocity, a relationship first suggested by Walter Merz.[4]

3.1 Acoustic Velocity as a Proxy for Domain Propagation

Direct measurement of domain wall velocity is complicated by a multitude of factors. Electrical measurements of global switching speeds are highly dependent upon equipment and measurement variables, such as electric field magnitude and rise time, circuit parasitics, and the abundance of types of domain walls. This makes understanding the ambiguous roles of material defects across all scales in dipole switching difficult, leading to broad interest in complementary data related to domain wall motion. Connections between ferroelectric domain wall velocity and acoustic velocity have been noted since Merz's work on barium titanate in the 1950's, remarking that switching speeds approach but do not surpass the speed of sound in the material.[4] If acoustic velocity serves as a ceiling for domain wall velocity, this phonon-dominated property and others like thermal conductivity may serve as useful proxies for better understanding effects of defects on ferroelectric switching.

To determine the validity of this hypothesis (that measurements of phonon behavior can be an effective proxy for domain wall mobility and pinning), phonon-dominated properties need to be measured in a material that possesses controlled defect populations across a wide spectrum of size scales. Lithium

tantalate again provides an opportune system for these measurements because of the availability of single crystals, tunable point defect populations, and crystallographic limitation to only antiparallel domains. Polarization vectors in this material align exclusively with the positive and negative *z*-axis, implying that phonon modes along the *c*-axis of $LiTaO_3$ play an important role in the site transition of lithium ions from either the $+z$ or $-z$ side of the nearest oxygen plane, the primary contributor to polarization in this system.[140] It has also been shown that domain walls in lithium tantalate lie within the *xz* plane (*x* walls) and *yz* plane (*y* walls), although there has been a reported preference for occupation of the *yz* plane.[57,120,141] A propagating domain wall progresses in a parallel direction to its plane normal in a manner typically referred to as sideways motion, implying that phonon modes that drive a domain wall in this fashion are also of primary interest for phonon velocity measurements.

3.2 Direct and Indirect Acoustic Phonon Velocity Characterization

The limited domain wall and polarization orientations in $LiTaO_3$ provide a limited set of directions of interest for phonon transport methods: the principal axes of the unit cell. Direct measurement of phonon group velocity was pursued via inelastic neutron scattering and speed of sound via ultrasonic transducers, and indirect quantification of phonon velocity was sought by measuring thermal conductivity on a selection of $LiTaO_3$ specimens having different cation ratios. These three different methodologies should allow for some cross-validation in an effort to test the hypothesis that phonon velocities as a simple proxy for maximum domain wall velocities can provide information about interactions of phonons and domain walls with point defect populations.

3.2.1 Inelastic Neutron Scattering

Inelastic coherent neutron scattering occurs when incident neutrons either gain or lose energy and/or momentum in the scattering process when they interact with lattice vibrations in the target material. When a monochromatic beam of neutrons is inelastically scattered, the amount of energy transfer that

occurs can vary, allowing detection of the scattered neutrons as a function of their scattered energy. The change in energy is equal to the quantized energy of the phonon, hν, that interacted with the neutron.

Determining the phonon energy and the scattering vector, q, requires that the neutron wavevector be known before and after the scattering event. The incident neutron wavevector, k_i, is chosen from a broad-spectrum (white) source by a monochromator such that the initial kinetic energy is larger than that of the phonons that are being measured. The monochromatic neutron beam is diffracted by the sample and both elastically and inelastically scattered neutrons with final wavevectors, k_f, are measured by the detector. The relationship between the phonon and neutron wavevectors is shown in Figure 3.1. In practical experiments, phonon dispersion curves are mapped in reciprocal space for a selected energy transfer by fixing either the reciprocal lattice vector or energy transfer value and scanning the unfixed parameter, i.e.: for constant-q scans, the reciprocal lattice vector being surveyed is fixed and energy space is scanned, and for constant energy scans, a given hν value is fixed and reciprocal space is scanned.

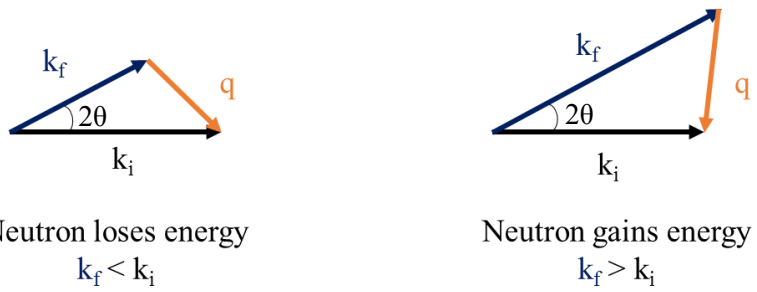

Figure 3.1: Vector triangles that describe inelastic neutron scattering where (left) the incident neutron loses energy ($k_f < k_i$) or (right) the incident neutron gains energy ($k_f > k_i$) during the scattering event that occurs. In either case the neutron possesses a scattering angle of 2θ and the scattering vector is defined by $q = k_f - k_i$.

The versatility of inelastic neutron scattering measurements allows for the detection of longitudinal and transverse acoustic and optical phonons. Longitudinal phonons describe lattice vibrations where atomic displacement is along the axis that the wave is travelling, where transverse phonons describe lattice vibrations where atoms are displaced along different axes than the one the phonon is propagating along. Acoustic phonons are low-energy phonons that displace neighboring atoms coherently and exhibit a linear relationship between frequency and wave-vector, where frequency trends toward zero at the center of the

Brillouin zone. Optical phonons, on the other hand, are higher energy phonons that result in out-of-phase movements of neighboring atoms that, in ionic crystals, can cause an electronic polarization that will couple to an electromagnetic field. Optical phonons are also distinguished from acoustic phonons in that they have a non-zero frequency at the Brillouin zone center

As discussed briefly in Chapter 3.1, only the phonon modes in lithium tantalate that most closely relate to domain wall motion are of interest in this study. Thanks to the limited domain wall orientations and mobilities in this system, the number of phonon modes that are of interest in this study are likewise limited. Acoustic phonons are of primary importance given the established link to acoustic velocity and ferroelectric switching speeds, and specifically acoustic phonon modes that participate in atomic displacements along the *z*-axis – the polar axis – and along the *x*- or *y*-axes – the directions of domain wall propagation. A schematic is given in Figure 3.2 showing the phonon modes that relate to these crystallographic axes in real space.

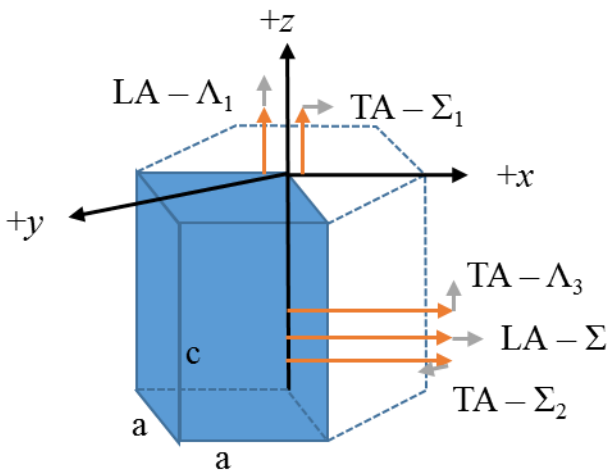

Figure 3.2: A graphical representation of the Σ and Λ phonon modes overlayed on a real-space hexagonal unit cell. For each labelled mode, orange arrows indicate the direction of phonon propagation and gray arrows indicate the direction of atomic displacement. Σ modes are characterized by displacement vectors in the *xy*-plane where Λ modes have displacement modes along the *z*-axis.

Inelastic neutron scattering experiments were completed on the HB3 Triple Axis Spectrometer at Oak Ridge National Laboratory with an incident energy of 14.7 meV. The Λ_3 transverse acoustic phonon mode was measured for SLT about the (3 0 ξ) reciprocal lattice point, which corresponds to atomic

displacement along the crystallographic *c*-axis. These measurements took place at both room temperature (RT) and 600 °C, which is well above the ~180 – 250 °C Debye temperature of LT where the individual intrinsic point defect species disperse, to examine the effect of the defect clusters vs dissociated defects.[142–144] A selection of energy sweeps at constant reciprocal lattice vectors are plotted in Figure 3.3. The energy value with the most intense signal for each of these scans was taken to be the band center for those reciprocal lattice vectors and used to determine the energy of the Λ_3 transverse acoustic phonon mode of stoichiometric vs congruent $LiTaO_3$ as reported by Chen *et al.*,[145] Friedrich *et al.*,[146] and Abrahams *et al.*[147] (Figure 3.4). The trends for phonon velocity show that the relatively defect-poor SLT exhibits an approximately 3x lower phonon velocity than that of the experimentally determined values for defect-rich CLT based on the magnitude of the slope as the bands near the (3 0 0) point.

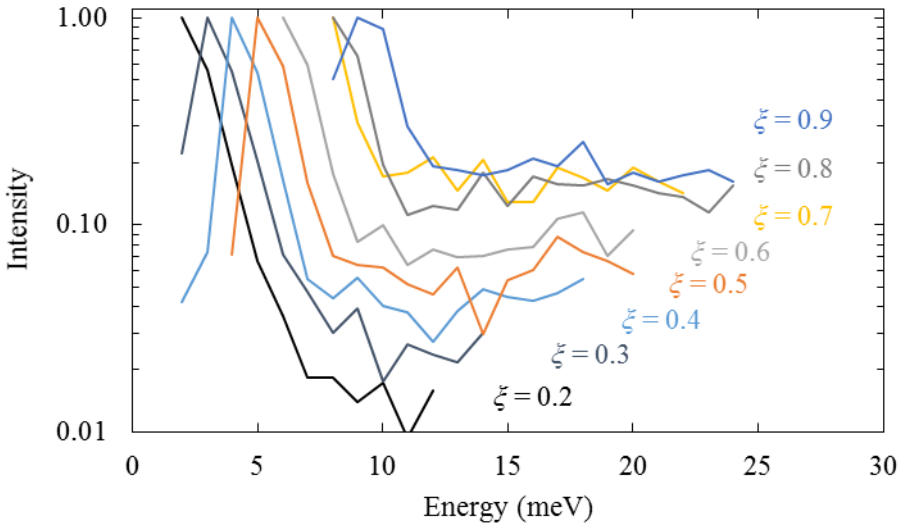

Figure 3.3: Inelastic neutron scattering scans at fixed wavevectors that search through energy space to determine the energy of the transverse acoustic (3 0 ξ) phonon branch.

Without directly measuring the phonon bands of CLT and SLT within the same experimental timeframe and parameters, it is difficult to accurately assign explanations for this stark difference in phonon velocity. An increase in many types of defect populations have typically been associated with an increase in phonon/defect scattering events that shorten mean free path for phonon transport, correlating to a decreased velocity.[148–155] If there is a random distribution of defects, this almost certainly is the case. Defect

species that preferentially align in some fashion, however, may not affect phonon velocities in a uniform manner. The nature of the point defect clusters in $LiTaO_3$ clustering together to neutralize charge, forming a tetrahedron of clustered defects aligned along the *c*-axis of the crystal as in Figure 3.5 (modelled after Kim *et al.*[86]), may impart a larger impact upon the phonons that control atomic movement along the *c*-axis. With measurements of only a single phonon band, this is largely conjecture. Further information on the defect concentration – acoustic velocity relationship in $LiTaO_3$ was sought through characterizing the transverse and shear speed of sound by application of ultrasonic transducers, which will be discussed in the following section.

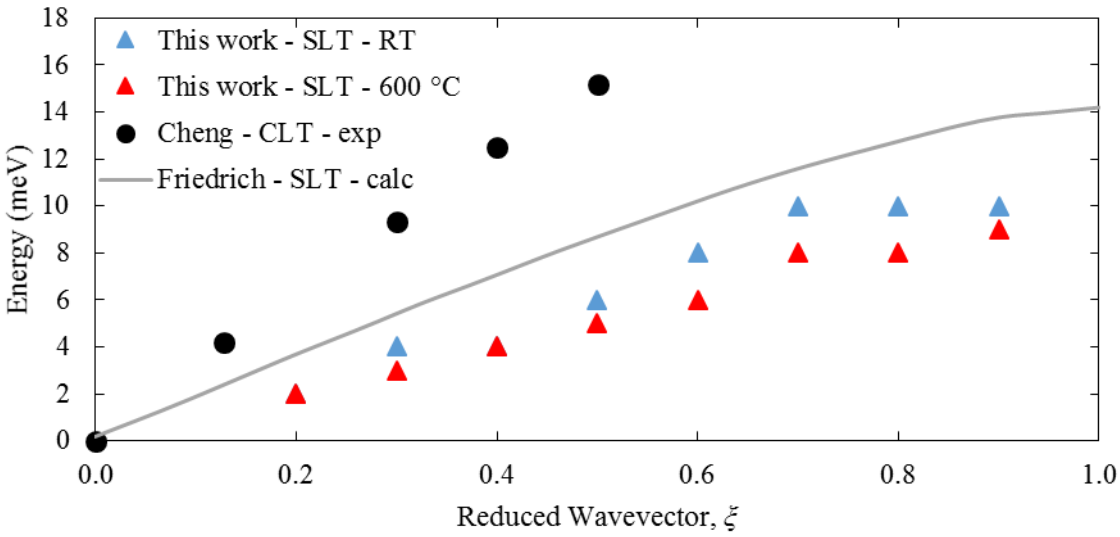

Figure 3.4: The transverse acoustic (3 0 ξ) phonon branch of stoichiometric as measured on the Triple Axis Spectrometer of the High Flux Isotope Reactor at Oak Ridge National Laboratory, as calculated by Friedrich *et al.* (2016), and congruent $LiTaO_3$ as reported by Cheng *et al.* (1993). The branch corresponding to SLT possesses a lower slope near the (3 0 0) point than the branch corresponding to CLT, indicating a higher phonon velocity in the defect-rich material. Reprinted with permission from Physica Status Solidi (b) Basic Solid State Physics and Journal of Physics: Consdensed Matter.

In comparing the room temperature and 600 °C data recorded on SLT it can be clearly seen that the phonon branch measured at high temperature possesses a lower velocity than the room temperature branch. A number of factors could be playing into this phenomenon: an increase in defect populations from the higher thermal energy, the intrinsic defect clusters break up above the Debye temperature and could shorten

the mean free path for phonon transport as a result,[142–144] or an increase in phonon-phonon (Umklapp) scattering as additional modes are populated with the higher thermal energy.

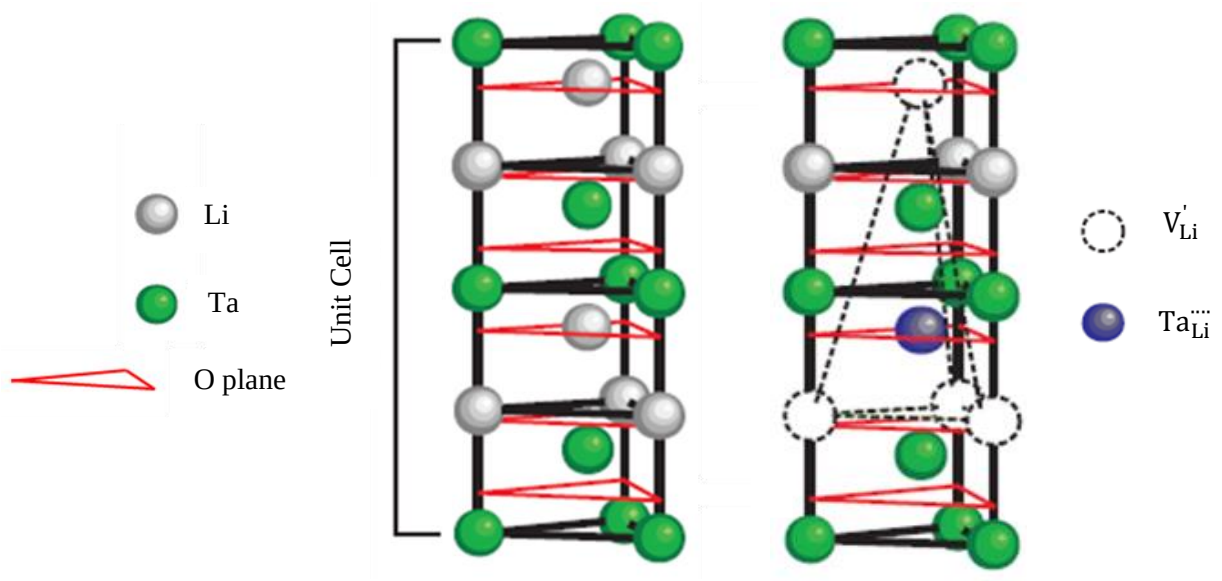

Figure 3.5: A depiction of the unit cell of $LiTaO_3$ both (right) with and (left) without its intrinsic point defect clusters after Kim *et al*. (2001). Reprinted with permission from Journal of Applied Physics.

3.2.2 Speed of Sound

Bulk speed of sound measurements via ultrasonic transducers were performed to determine global acoustic velocities to supplement the information gained in the inelastic neutron scattering experiments. In these experiments longitudinal and shear wave transducers were held in contact with the surface of three $LiTaO_3$ single crystals that possess different cation ratios, as inferred by T_C measurements, and pulsed ultrasonic vibrations were timed as they made their way through the thickness of the crystals, bounced off the opposite crystal surface, and returned to the transducers. The transit time along with precise knowledge of sample thickness allows the speed of sound to be calculated for a given mode (longitudinal vs shear wave) along the measured crystal axis.

Three *z*-cut $LiTaO_3$ single crystals with distinct chemistries were used to examine the effects of point defect concentrations on longitudinal and shear acoustic velocity at room temperature. These data, plotted in Figure 3.6, indicate that the point defects of $LiTaO_3$ have a disparate effect on the velocity of the

modes studied. The total change in longitudinal velocity between the congruent and near-stoichiometric compositions measured is approximately 524 m/s as opposed to a 29 m/s change between the same compositions for shear velocity. The change in longitudinal velocity follows a similar trend to that presented in the inelastic neutron data: as Li_2O concentrations decrease (and point defect concentrations correspondingly increase), acoustic velocity increases. These data corroborate the apparent increase in phonon velocity with increasing point defect content among phonons where ion displacement occurs along the *z*-axis and provide new insight into the anisotropic role that these defects play in phonon transport in this material. Even though the inelastic neutron scattering data and transducer measurements agree, they do not provide enough information to satisfactorily say whether or not acoustic velocities can act as a potential

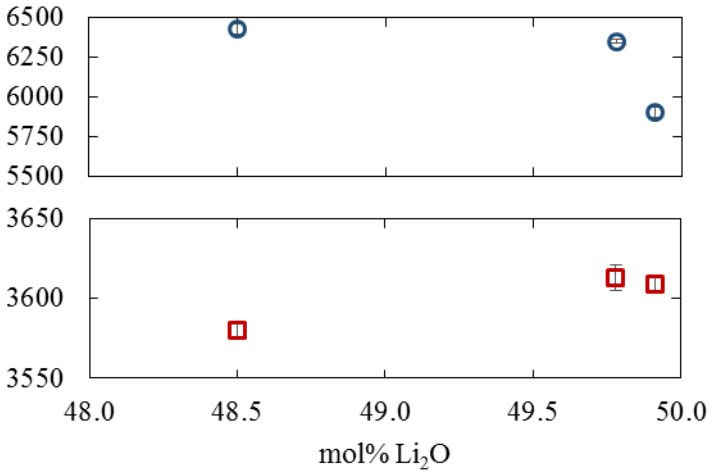

Figure 3.6: (Upper) Longitudinal and (lower) shear acoustic velocities for lithium tantalate single crystals of three distinct chemistries collected at room temperature.

surrogate for domain wall velocity measurements due to incomplete datasets along both the *z*- and the *x*- or *y*-axes for multiple $LiTaO_3$ chemistries.

3.2.3 Thermal Conductivity

Another method of investigating phonon propagation is measuring thermal conductivity, which is particularly relevant in dielectric materials, as the role of lattice vibrations in carrying heat outweighs any contributions from mobile charge carriers.[156–158] The impact of point defect concentrations on thermal

conductivity has been studied in a variety of materials, and in general it is found that mass impurities – from substitutional atoms to vacant lattice sites – decrease thermal conductivity.[148,149,151,153–155,159–161] A handful of experiments examining thermal conductivity in $LiTaO_3$ at the congruent and stoichiometric compositions have been reported, but little work has addressed the chemistry range between those compositions.[97–99] In this work thermal conductivity data from frequency domain thermoreflectance (FDTR) and time domain thermoreflectance (TDTR) measurements are reported.

These techniques utilize an optical laser pump-/probe assembly that extracts material thermal properties from the phase response of the thermal wave over a range of frequencies to determine the thermal conductivity. FDTR employs a sinusoidally modulated, continuous wave pump beam that produces time-harmonic heating that causes surface temperature oscillations at the chosen modulation frequency. The amplitude and phase of surface temperature rise are measured in relation to pump beam frequency by a second, continuous wave probe beam. In TDTR, the pump beam is modulated by a femtosecond laser that operates at a high frequency. The heating rate in TDTR is not time-harmonic, however, and is made up of several frequency components. The pulsed probe beam in this technique is derived from the source laser and delayed with respect to the pulses of the pump beam by a mechanical delay line. More detailed

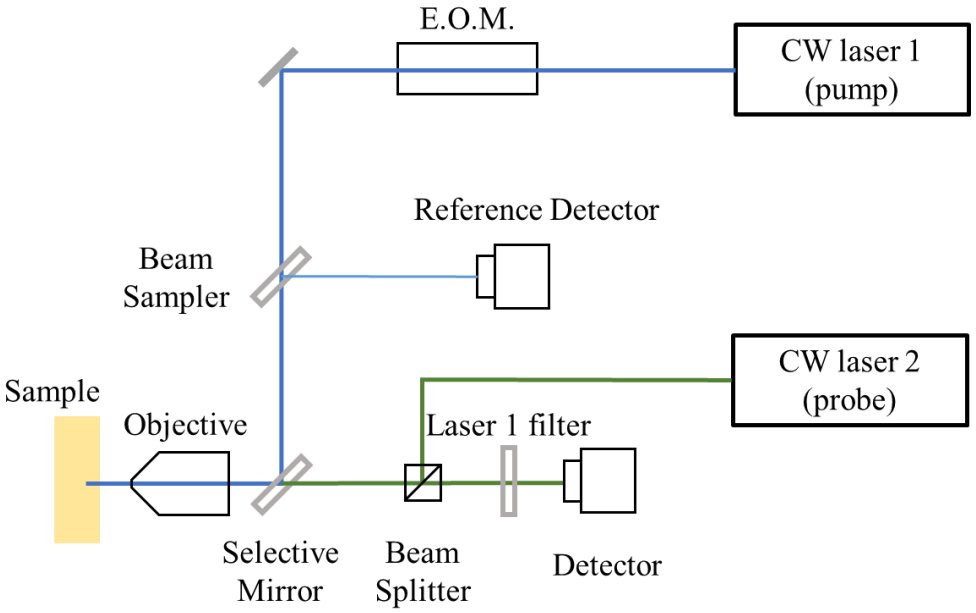

Figure 3.7: A schematic representation of the FDTR setup used in these experiments after Schmidt *et al.* (2009). Reprinted with permission from Review of Scientific Instruments.

discussion of the FDTR and TDTR techniques can be found in Schmidt *et al.*[162] and Cahill,[163] respectively, although an experimental layout for the FDTR setup used in these experiments is provided in Figure 3.7.

Thermal conductivity data were collected from $LiTaO_3$ *z*-cut single crystals of different compositions, identical to those reported in Chapter 2 of this thesis. An 80 nm layer of gold was thermally evaporated onto the surface of the $LiTaO_3$ single crystals as well as sapphire and single-crystal silicon witness wafers for calibration. This Au acted as a thermal transducer for the thermoreflectance measurements, absorbing a known fraction of the incident laser energy and subsequently serving as a known source of thermal energy. Literature values were used for the thermal conductivity of Au as well as the volumetric heat capacities (C_v) of Au, CLT and SLT.[164,165] The VTE treated crystals were assumed to have a $C_v = 3.00 \times 10^6$ J/m^{3}K.[165] Thermal conductivities were fitted simultaneously with the thermal boundary conductance (TBC) between the Au transducer and substrate. The uncertainty for the FDTR data was calculated based on 95% confidence bounds from the random spots and ± 2nm uncertainty associated with the transducer thickness. The samples were then exposed to a pump laser at room temperature for sufficient times to induce a steady-state temperature rise. This was measured by a probe beam that detects the resulting change in reflectance, which is proportional to the change in temperature at the sample surface. These techniques and their setups are described in further detail by Schmidt *et al.*[162] and Cheaito *et al.*[166]

The thermal conductivity data from this work are plotted in Figure 3.8 alongside that of CLT and SLT as reported by Hum *et al.*[97] and Nakamura *et al.*[98] who used a conventional laser flash technique to acquire their data. All four presented datasets exhibit an increasing thermal conductivity as Li_2O content increases from the CLT composition to the SLT composition and point defect concentrations decrease. Thermal conductivities from the thermoreflectance methods are between one third and one half lower in magnitude than that measured by laser flash. The upward trend in thermal conductivity with decreasing defect concentration found here represents an acoustic velocity trend that directly contradicts that from the longitudinal speed of sound and inelastic neutron measurements previously presented.

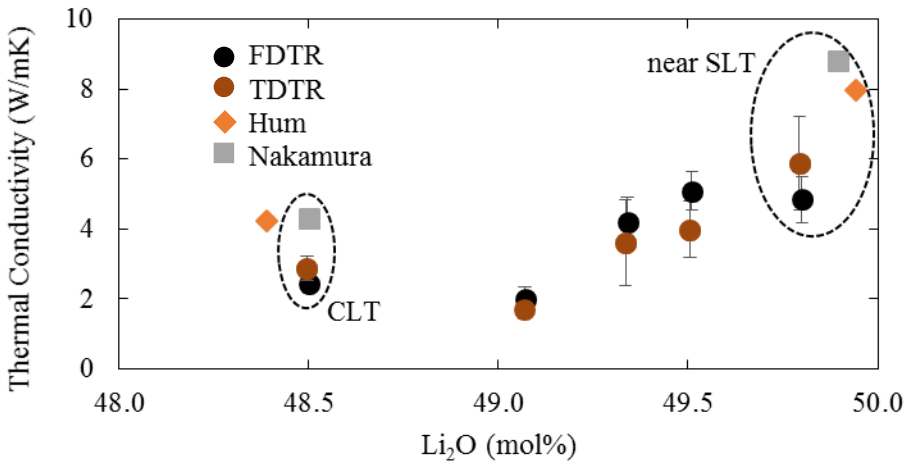

Figure 3.8: Thermal conductivity of *z*-cut $LiTaO_3$ single crystals as a function of lithium oxide content.

3.3 Summary

All three of the techniques presented in this chapter measured phonon displacement along the *z*-axis of $LiTaO_3$ single crystals. Inelastic neutron scattering and speed of sound measurements indicate a trend in acoustic velocity that disagrees with classic phonon transport theory: that acoustic phonons scatter off lattice defects resulting in a decreased acoustic velocity. These two methods signify an acoustic velocity along the *z*-axis that increases with increasing defect populations. Thermal conductivity data, however, decreases in these materials as point defect populations increase. The disagreement between the various direct and indirect methods of quantifying acoustic velocity in $LiTaO_3$ as a function of point defect concentrations make it impossible to say with any certainty that acoustic velocity can act as an approximation of domain wall velocity in this system.

CHAPTER FOUR

PRESSURELESS SINTERING OF $LiTaO_3$ VIA ATMOSPHERE CONTROL

Quantifying the effects of grain boundaries on ferroelectric switching behavior requires polycrystalline specimens. While $LiTO_3$ single crystals are widely available, reports of polycrystalline samples are very limited. As discussed throughout this document, there are two large factors that must be overcome to produce highly dense lithium tantalate polycrystals: disparate ionic mobilities and an anisotropic coefficient of thermal expansion. This chapter discusses the work done to overcome these obstacles to produce polycrystalline lithium tantalate that is highly dense and phase pure – a first in the literature.

4.1 Processing Techniques for Sintering and Densification

Addressing the two issues outlined above was attempted through two distinct processing techniques. To overcome sintering stresses generated by anisotropic CTEs, producing polycrystalline parts that possess a textured microstructure, aligning grain orientations such that their *c*-axes are aligned, was attempted through application of templated grain growth via tape casting. Orientation control of the *a*- and *b*-axes is not a matter of great concern within the *xy* plane given that these two axes have identical CTE values. To overcome challenges presented by ions with large differences in ionic mobility, a study to investigate the effect of Li_2O overpressure – to control lithium vacancy concentrations – on densification and grain size was performed.

4.1.1 Templated Grain Growth

Anisotropy in thermal expansion coefficient was addressed in this system by texturing the microstructure of these samples. Texture of bulk polycrystals has been achieved before by applying templated grain growth (TGG) to the tape casting forming method, as schematically shown in Figure 4.1 after Mistler *et al*.[167,168] In this technique a slurry is prepared that contains a bimodal particle size distribution, up to 95% of which is composed of small, equiaxed particles and the remainder are large,

anisometric single crystals which are intended to template grain growth during sintering. The templating particles are initially randomly oriented in the dispersion, but during the casting portion of the process, the doctor blades impart a shear force that aligns the templates parallel with the casting direction to achieve the desired texture for the dense part. During sintering the seed crystals coarsen at the expense of the fine powder particles that make up the rest of the matrix and produce a coarse-grained microstructure that is textured in the plane-normal direction. This is exemplified in Figure 4.2 by Meier *et al*. in the $BaTiO_3$ system, showing coarsening of templated samples as a function of thermal treatment.[168] Diffraction data can then be used to determine the level of texturing that was achieved by calculation of a Lotgering factor, a simple and informative but imperfect measurement of the texture of a sample.[169–171] The Lotgering factor is calculated by determining the ratio of integrated intensities for the peak of interest in the textured system to that of the same peak in a randomly oriented microstructure as given in the equations below for the case of ‹0 0 *l*›-texture:

$$f_{(00l)} = \frac{P_{(00l)} - P_o}{1 - P_o} \tag{4.1}$$

where

$$P_{(00l)} = \frac{\sum I_{(00l)}}{I_{(hkl)}} \tag{4.2}$$

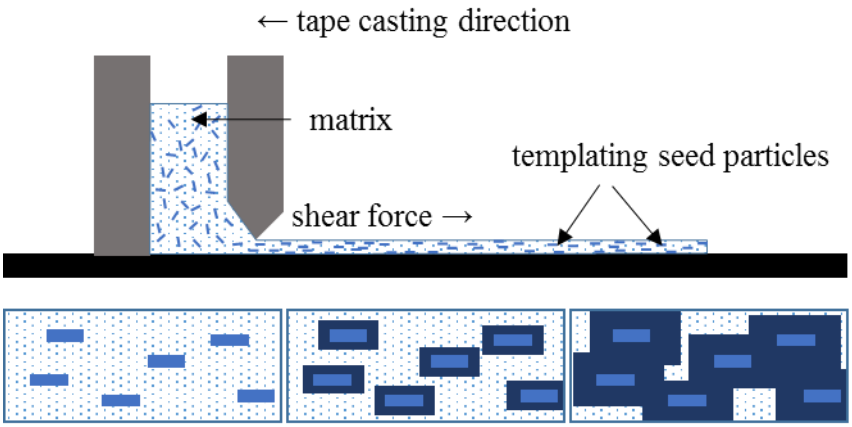

Figure 4.1: (Top) A schematic of the templating process by tape casting to texture a polycrystalline ceramic body. (Bottom) From left to right – as the duration and intensity of heat treatment increases – the texture fraction increases.

$$P_o = \frac{\sum I_{o(00l)}}{I_{o(hkl)}} \tag{4.3}$$

$\Sigma I_{(00l)}$ is the summation of the XRD peak intensities of all the (0 0 *l*) peaks in the textured sample pattern and $\Sigma I_{(hkl)}$ is the summation of the peak intensities for all (*h k l*) peaks that appear in the pattern. The $\Sigma I_{o(00l)}$ and $\Sigma I_{o(hkl)}$ values are summations of the peak intensities for a sample with a randomly oriented microstructure.

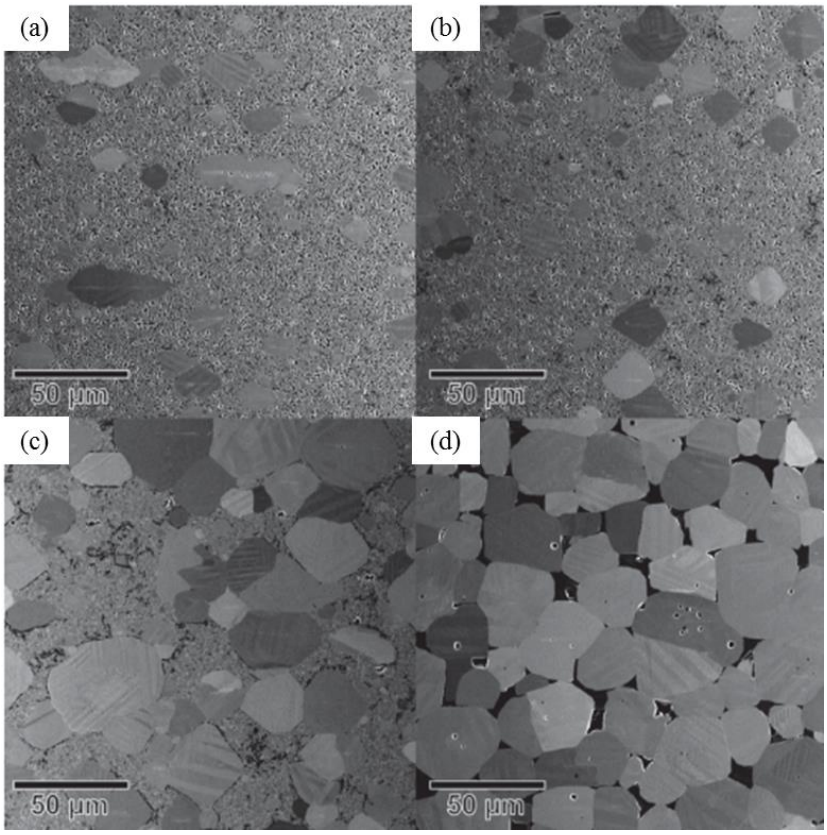

Figure 4.2: Microstructures of templated $BaTiO_3$ after sintering at (a) 1275 °C for 24 hr, (b) 1300 °C for 12 hr, (c) 1300 °C for 24 hr, and (d) 1325 °C for 12 hr. Reprinted from Meier *et al.* (2016) with permission from Journal of the American Ceramic Society.

In this material system, texturing polycrystalline samples such that the *c*-axis is aligned with the out-of-plane direction of a cast tape is an ideal orientation. This is true for two reasons, the first of which is that CTE values of the *a*- and *b*-axes are identical but differ by a factor of 4 with the CTE of the *c*-axis ($\alpha_a = \alpha_b = 16 \times 10^{-6}/°C$, $\alpha_c = 4 \times 10^{-6}/°C$) meaning that controlling the in-plane orientation of the seed crystals

is largely unnecessary. The second reason is that the only possible ferroelectric polar transition is along the *c*-axis, so application of an electric field along the c-axis is required to investigate ferroelectric switching.

4.1.2 Manipulation of Atmosphere to Influence Sintering

It is typical for bulk diffusion to be the rate limiting step in sintering of oxide materials by the slowest diffusing ionic species along its fastest pathway.[172] Fielitz *et. al*[173] compiled a series of diffusion studies in $LiNbO_3$ and $LiTaO_3$ that calculated various self diffusion, interdiffusion, and tracer diffusion coefficients which are shown in Figure 4.3. It is important to note that in the studies that examine either Nb or Ta diffusion in their non-native material, the diffusion coefficients for the group 5 cations are taken by the authors of the original studies to representative of the diffusion for Nb in $LiNbO_3$ and Ta in $LiTaO_3$ because of the similarity of the Nb^{5+} and Ta^{5+} ions. From these reports, it is likely that tantalum is the slowest diffusing ion in these materials. The data shown in Fig. 4.3 also indicate that tantalum diffusion is heavily dependent on cation stoichiometry, dropping two to three orders of magnitude as lithium content is increased from the congruent to the stoichiometric composition in $LiNbO_3$, indicating that lithium vacancies provide pathways for tantalum diffusion – a conclusion supported by experimental and DFT literature.[87,173,174] If tantalum diffuses along Li vacancies, modifying lithium vacancy concentrations is one method to control Ta diffusion.

Atmospheric control is one mechanism that can be used to influence ionic mobility in ceramics. In systems that are diffusion-limited by oxygen transport, it is common practice to create oxygen vacancies by sintering in a reducing atmosphere. We have demonstrated that vapor transport equilibration can control lithium vacancy concentrations in single crystals and so have chosen to adapt that technique to sintering experiments to examine the role of lithium vacancies in sintering of $LiTaO_3$.

4.2 Batching and Forming

Equimolar amounts of lithium carbonate (Li_2CO_3, JT Baker Chemical CO., 99.9 %) and tantalum oxide (Ta_2O_5, Alfa Aesar, 99%) were mixed on a planetary mill for one hour in ethanol, dried and calcined

at 1000 °C for ten hours in air to form single-phase $LiTaO_3$, which was later confirmed by XRD (Figure 4.4). The primary particle size of this powder was found to be 850 nm with a standard deviation of 420 nm via laser particle size analysis.

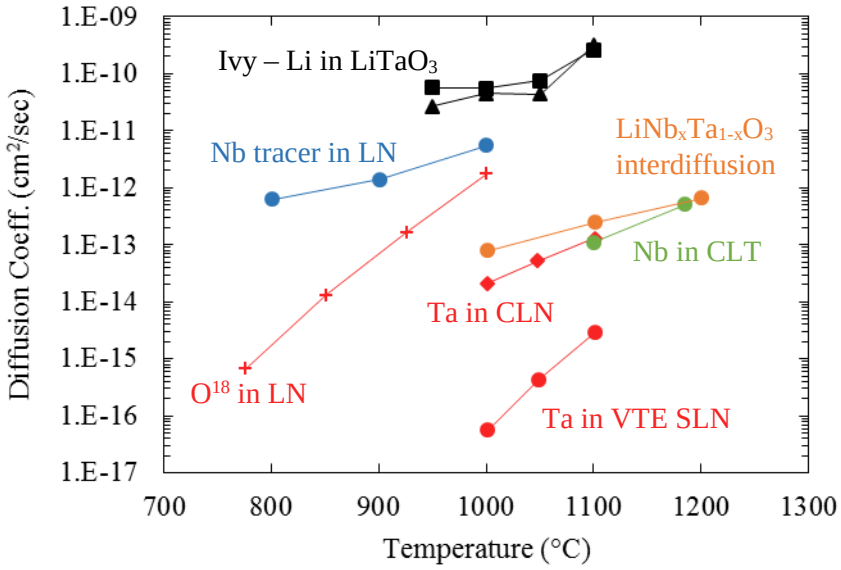

Figure 4.3: Self, tracer, and interdiffusion coefficients for ionic species in $LiTaO_3$ and $LiNbO_3$ single crystals after Fielitz, *et. al.* (2014). Heavy cation species show the lowest diffusion coefficients at any given temperature, but it is interesting to note that Ta diffusion in $LiNbO_3$ is decreased by 2-3 orders of magnitude in a VTE-treated, stoichiometric $LiNbO_3$ vs congruent $LiNbO_3$. Reprinted with permission from Solid State Ionics.

An aqueous slurry was pursued for chemical safety and ease-of-handling considerations. In contrast to earlier studies,[121,123–125] discrete sintering aids were avoided to focus on intrinsic diffusion mechanisms. A stable slurry with solids loading of 45 vol% $LiTaO_3$ was achieved with the incorporation of 7 vol% Darvan 821A used as a dispersant, 3 vol% high molecular weight polyvinyl alcohol (average m.w. 88,000-97,000 g/mol, 98-99% hydrolyzed) as a binding agent, and 45 vol% deionized H_2O. This specific formulation allowed for the highest solids loading that was achieved in a stable slurry. The slurry components were mixed sequentially on a high speed mixer (FlackTek, Inc., DAC 150.1 FVZ-K) for three minutes at 1200 rpm and three minutes at 600 rpm. The slurry was cast on a mylar sheet at ~540 µm thickness and allowed to dry in open air. The green $LiTaO_3$ tape was then sectioned and prepared for sintering.

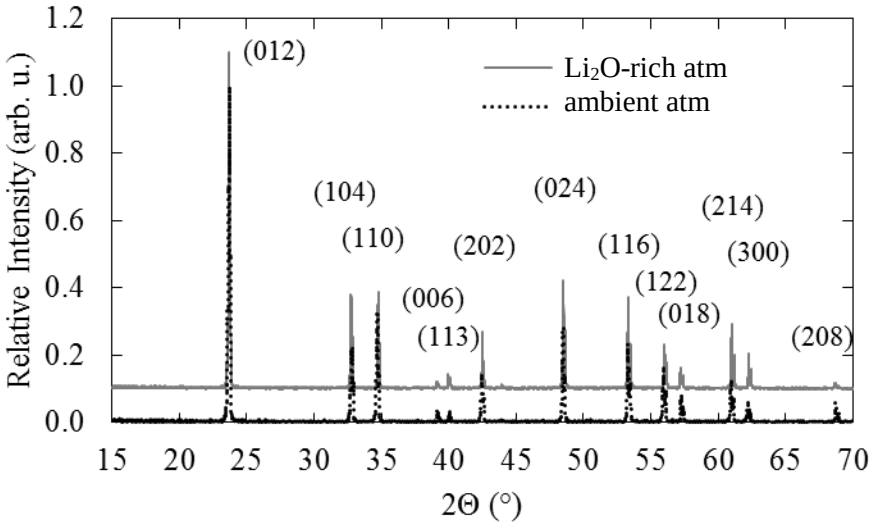

Figure 4.4: X-ray powder diffraction patterns for two representative $LiTaO_3$ polycrystalline samples. The solid gray line represents a specimen sintered in a Li_2O-rich atmosphere and the dotted black line represents a specimen sintered in an unaltered, ambient atmosphere.

4.3 Role of Gaseous Li_2O on Densification of Randomly Oriented $LiTaO_3$

Specimens of $LiTaO_3$ tape were sintered at 1250, 1300, and 1350 °C for six, eight, and ten hours under two differing atmospheric conditions: one consisting of a sample enclosed in a crucible with a static air environment and another consisting of a sample buried in a Li_2O source powder, again covered with a crucible to maintain a Li_2O vapor overpressure. The lithium oxide powder source is made of a mixture of 40 mol% $LiTaO_3$ + 60 mol% Li_3TaO_4, the thermal decomposition of which yields Li_2O(g) and $LiTaO_3$ until the reaction self-terminates when the powder is compositionally in equilibrium with the $LiTaO_3$ phase. Samples sintered in the Li_2O-rich atmosphere were fully buried in the two-phase powder with corrugated platinum foil spacers to prevent the burial powder from bonding directly to the specimens while still allowing vapor transport to occur. The tape cast specimens, spacers, and powder were loosely covered during thermal processing by a platinum crucible to aid in controlling the atmospheric pressure of the evolved Li_2O.

The lattice parameters of tapes sintered under the two tested atmospheric conditions were investigated via x-ray diffraction on a Panalytical PW3040 X-Ray Diffractometer. The diffraction patterns are provided in Figure 4.4 and indicate a randomly oriented microstructure and an R3c crystal symmetry.

The lattice constants of these samples, which are listed in Table 4.1, show that the sample sintered in the Li_2O-rich atmosphere possesses a unit cell that is 0.31% smaller in volume than the sample sintered in an unadulterated air atmosphere, and specifically possesses a 0.11% smaller a-axis and a 0.09% smaller c-axis. Table 4.1 also contains lattice parameters for sister-samples of the stoichiometric and congruent single crystals used in the earlier chapters of this thesis. These values were obtained from crushed specimens that were measured at the Advanced Photon Source at Argonne National Laboratory on beamline 11-BM. The lattice parameters from the commercial single crystals are between 0.0063 and 0.017 Å smaller than comparable lattice constants for the polycrystalline samples. It is interesting to note that the unit cell volume of the stoichiometric crystal is 0.18% smaller than the congruent crystal, which is something that was previously noted by Barns *et. al.*[175] Quantifying Li content via this approach would require deconvoluting the effects of residual stresses within the polycrystalline samples, but a simple qualitative comparison of the trends in unit cell volume is consistent with the specimen sintered in air having a lower lithium content than the one sintered in $LiTaO_3$-Li_3TaO_4 burial powder.

Table 4.1: Lattice parameters for polycrystalline $LiTaO_3$ samples as a function of sintering atmosphere and lattice parameters for CLT and SLT single crystals.

	SLT single crystal	CLT single crystal	Li-rich atm polycrystal	Ambient atm polycrystal
a (Å)	5.1507	5.1539	5.1602	5.1660
c (Å)	13.7751	13.7824	13.7795	13.7918

Temperature-dependent impedance data were collected using an HP 4294A impedance analyzer with a 500 mV oscillator from 1 kHz – 1 MHz. DuPont 4922N silver paste was used for the electrode material and cured for one hour at 100 °C before the measurements were performed. These specimens were heated and cooled at a rate of 2 °C/min under ambient atmospheric conditions and a short circuit configuration. These data, recorded upon heating, are provided in Figure 4.5 and show permittivity curves for lithium tantalate polycrystals that were sintered at 1300 °C for ten hours, one under an ambient atmosphere and another under a Li_2O-rich atmosphere, alongside data from a commercially produced, congruent single crystal that is used as a reference point. The congruent single crystal and ambient-

atmosphere polycrystal possess a Curie temperature of ~ 601 °C while the Li_2O-rich atmosphere specimen has a T_C of ~ 665 °C, which, as established in Chapters 1 and 3, is directly related to Li_2O content in single crystals.[63,66,109,176] These data, along with the difference in unit cell volume, indicate that the atmospheric conditions present during sintering can have a measurable impact on the final chemistry of the sample: in these two samples that were produced from the same batch and have the same (stoichiometric) batch chemistry, sintering $LiTaO_3$ under an atmosphere where Li_2O is present has a VTE-like effect and prevents lithium volatilization from the tape cast specimens, preserving stoichiometry in much the same way that PbO loss in lead-based perovskites is managed during sintering.[172,177]

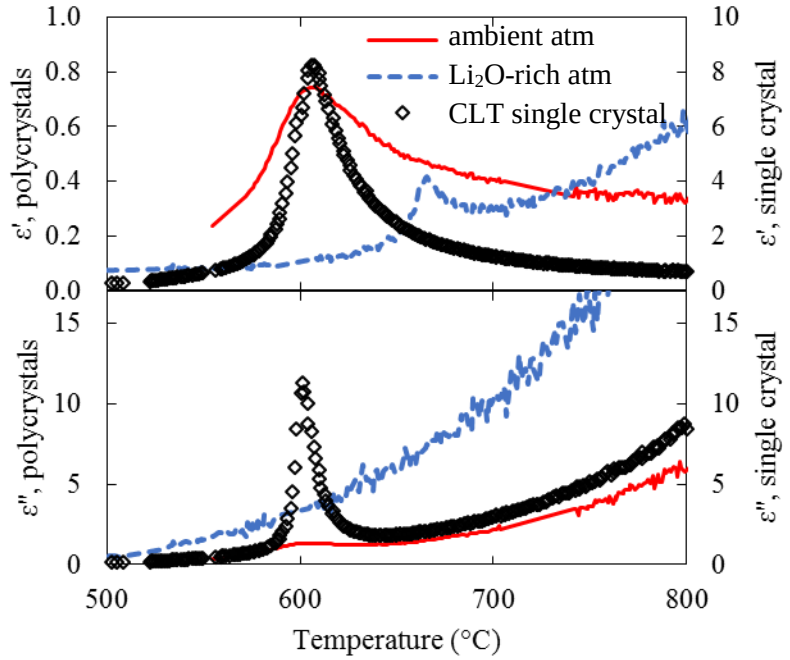

Figure 4.5: (Upper) Real and (lower) imaginary permittivity for $LiTaO_3$ polycrystalline samples sintered under two different atmospheric conditions. Data collected on a commercial, congruent sample is provided for comparison.

Scanning electron microscopy was performed using an FEI Quanta 600I Environmental SEM for additional microstructural characterization. After deposition of a conductive Au-Pd layer, the as-sintered and fractured cross sections (Figure 4.6) of all samples were imaged in both backscatter and secondary electron modes with an accelerating voltage of 20 kV and a working distance of ~ 12 mm. Significant thermal stresses from the anisotropic CTE ($\alpha_a = 16 \times 10^{-6}$/°C, $\alpha_c = 4 \times 10^{-6}$/°C) resulted in large amounts of

stress cracking and grain pullout during the polishing process. This made determining grain boundaries at the polished surface difficult and added significant uncertainty to grain size values. It was eventually decided that fracture surfaces would be used for grain size characterization. It is worth noting that the thin sample geometry would lead to minimal thermal gradients during sintering. The procedures from ASTM E112-13 were used for lineal intercept analysis to determine grain size as a function of sintering time, temperature, and atmosphere as a function of sintering conditions.

Examination of the microstructures of these samples revealed common indicators of abnormal grain growth (AGG) present in the samples sintered in an ambient air atmosphere. The fracture surfaces of these samples show a higher fraction of grains with entrapped porosity compared to the fracture surfaces sintered in the Li_2O-rich atmosphere for all time and temperature combinations. Porosity within grains – as opposed to lying at a grain boundary – was observed significantly less frequently in images of the as-sintered surfaces. Quantifying the amount of entrapped porosity by lineal intercept analysis of the micrographs is difficult in images of fracture surfaces due to their roughness, although in Figure 4.6 the amount of grains showing intragranular porosity is 3.6x greater in 4.6a vs 4.6b, 16x greater for the specimen in 4.6c vs 4.6d, and 5x greater in 4.6e vs 4.6f. To determine whether a grain possessed intragranular porosity, any evident pores needed to be nearly spherical in morphology – due to minimization of surface energy between the pore and bulk grain – and obviously residing away from a grain boundary. If any pores were not spherical or if there was any doubt regarding the nature of the pores location in relation to a grain boundary, it did not contribute to the count of grains containing pores. Measurements of density via the Archimedes fluid displacement technique corroborated the porosity observations from the micrographs in that samples sintered in the burial powder reached relative densities of up to 95% while those sintered without burial powder did not exceed 91% density.

The grain size analysis data from the fractured cross sections of $LiTaO_3$ tapes is given in Figure 4.7. There are not many significant relationships to be observed in grain diameter as a function of time and temperature, although the general trends of higher temperatures and longer sintering times yield larger grain

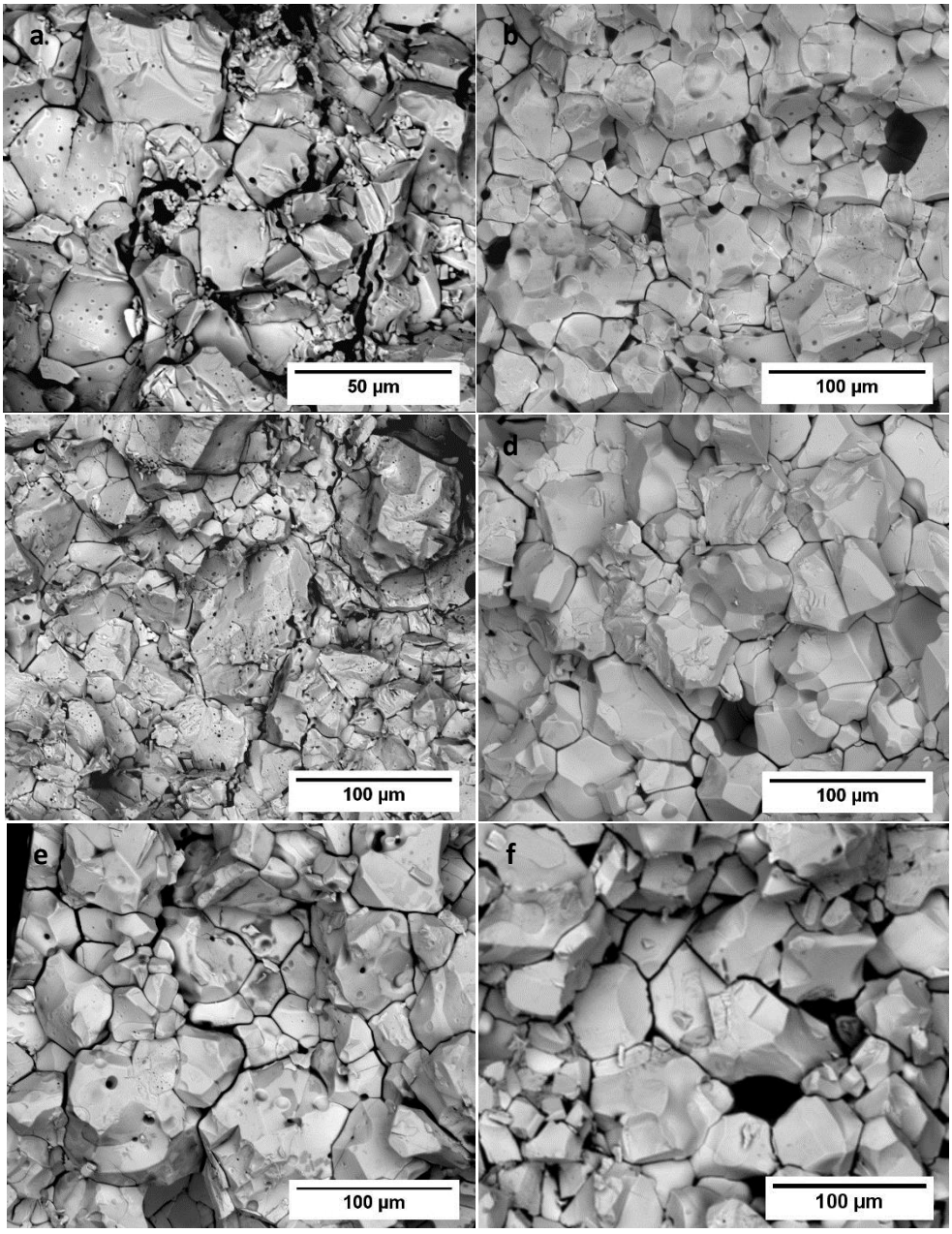

Figure 4.6: Fracture surfaces of polycrystalline $LiTaO_3$ specimens that were sintered for ten hours under the following temperature and atmosphere conditions: a) 1250 °C – air, b) 1250 °C – Li_2O, c) 1300 °C – air, d) 1300 °C – Li_2O, e) 1350 °C – air, f) 1350 °C – Li_2O.

sizes seems to hold true. The effect of the two sintering atmospheres examined here on grain size is small, although average grain sizes are slightly larger for specimens sintered in Li_2O-rich atmospheres as opposed to ambient atmospheres for a given sintering time. An interesting data subset is the samples sintered in air for six hours: the spread in grain size as a function of temperature is much wider for this atmosphere and sintering time combination that the others which may also point to abnormal grain growth. If AGG is occurring in this system as theorized, relatively short sintering times would reveal it more readily than long sintering times due to normal grain growth eventually catching up with abnormal grains that were pinned after coming into contact with other abnormal grains during growth.[172] That the short sintering time data subset possesses a significantly more narrow grain size spread for the samples sintered in a Li_2O-rich atmosphere implies that lithium deficiency could play a primary role in sintering behavior – a hypothesis that was introduced Chapter 4.1.2.

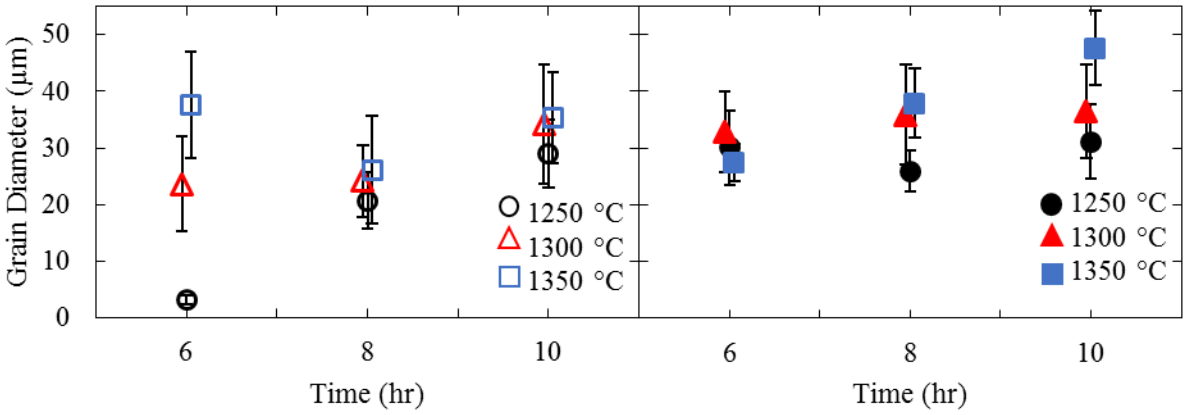

Figure 4.7: (Left – ambient atmosphere, right – Li_2O-rich atmosphere) Grain size of $LiTaO_3$ as a function of sintering time, temperature and atmosphere.

When considering dominant sintering mechanisms in this system, it is important to keep the defect chemistry of $LiTaO_3$ in mind and how the relationship between lithium vacancy concentration and tantalum mobility may affect the various densifying and non-densifying mechanisms in play. The six sintering mechanisms of consolidated crystalline bodies are given in Figure 4.8 below after Rahaman.[172] Of these different mechanisms, only 1-3 contribute to densification, although all six cause the necks between distinct particles and thus influence the rate of densification.

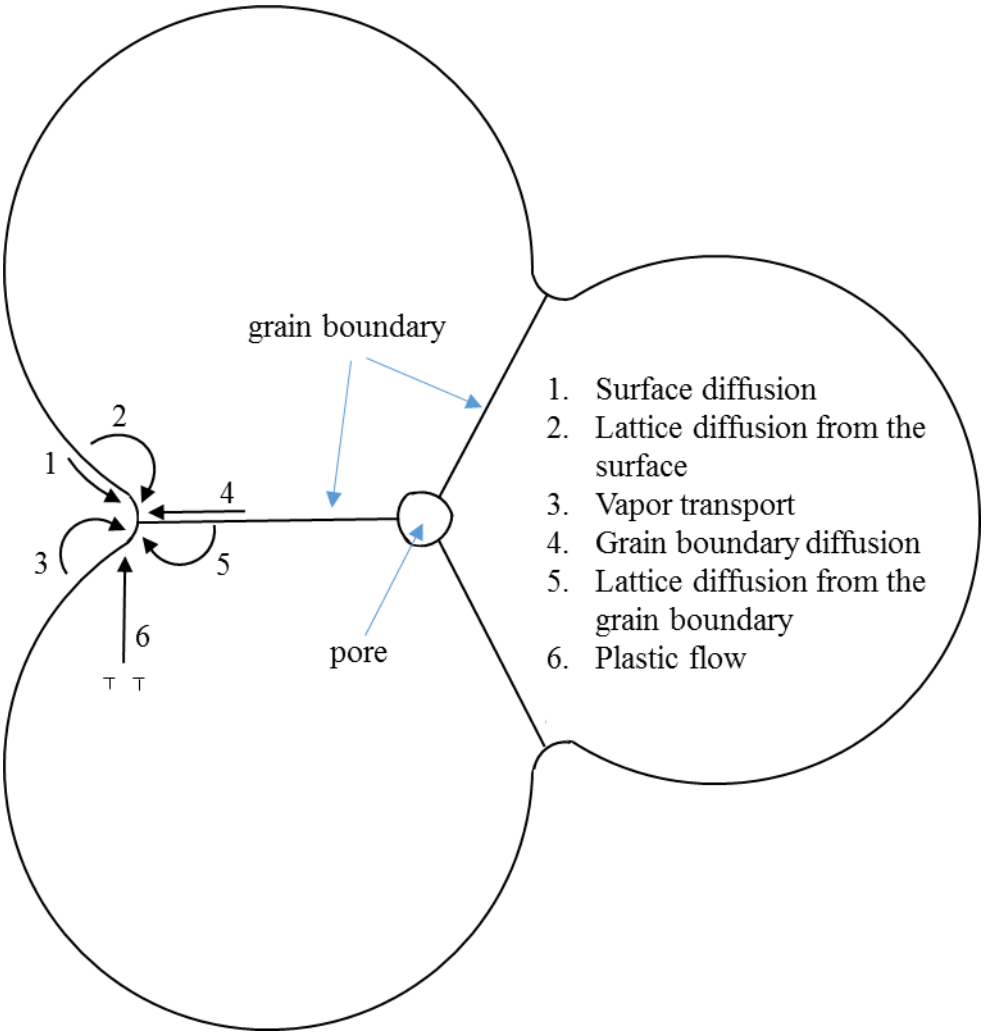

Figure 4.8: There are six distinct mechanisms by which a consolidated group of particles can be sintered together. (1) Surface diffusion, (2) lattice diffusion from a surface, and (3) vapor transport lead to densification of the consolidated body while (4) grain boundary diffusion, (5) lattice diffusion from the grain boundary, and (6) plastic flow do not contribute to densification.

In this specific experiment, it is likely that plastic flow is not a relevant densifying mechanism because an external force is not being utilized to achieve densification, such as in hot pressing. If vapor diffusion, a non-densifying mechanism, was dominant here it is likely that samples sintered in an atmosphere with excess Li_2O present would have lower densities than those sintered in air, which is not observed in density measurements. Similarly, if non-densifying lattice diffusion were to have a large impact in this system, it could be assumed that increasing the available lattice sites for tantalum ions to pass through (i.e., increasing lithium vacancy concentration) would lead to lower density samples when processed in

Li_2O-rich atmospheres. It was observed that a high degree of non-densifying surface diffusion was present in samples sintered in air, as indicated in the micrograph shown in Figure 4.9, which was not present in samples buried in a Li_2O source. Increased surface diffusion present in samples where an overpressure of Li_2O was not maintained could point to lithium losses actively occurring during sintering which would imply creation of lithium vacancies at the surface of these materials. This phenomenon would not contribute to the densifying grain boundary diffusion mechanism, particularly given that, again, higher densities were achieved and fewer indicators of abnormal grain growth were observed in samples sintered with a Li_2O overpressure. If, however, the lithium vacancies that were formed at surfaces due to lithium evolution were to transport into the bulk of a grain they would then contribute to the non-densifying diffusion mechanism of lattice diffusion from a surface. This process may help explain why there are an increased number of markers for abnormal grain growth (intragranular porosity and a wider disparity in grain sizes for short sintering times) and lower densities in $LiTaO_3$ samples that were sintered in air vs those sintered in an atmosphere containing excess Li_2O.

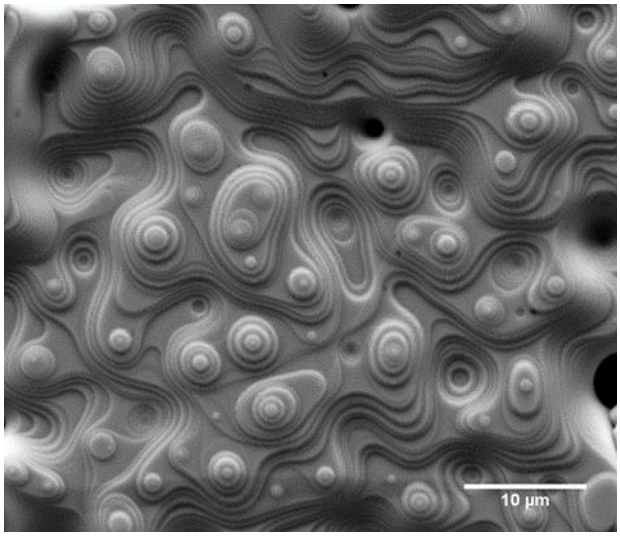

Figure 4.9: A micrograph of a polycrystalline $LiTaO_3$ sample sintered in ambient air in a two-stage approach of 1300 °C for ten minutes followed by 1225 °C for twelve hours. The sharp terracing evident here is indicative of a large degree of surface diffusion.

4.4 Templated Grain Growth in $LiTaO_3$

Tape casting experiments incorporating seed crystals that were chosen to provide a *c*-axis texture were informed by the earlier experiments with unseeded lithium tantalate tape cast samples. Templating seed crystals with an approximate aspect ratio of 10:1 were produced from crushed 60 μm thick wafers of *z*-cut $LiTaO_3$ purchased from NanoLN, a single crystal manufacturer that specializes in thin $LiNbO_3$ and $LiTaO_3$ wafers. Seeded slurries were composed of 14 mol% seeds, 84 mol% $LiTaO_3$ powder, and 2 mol% MgF_2, which was used as a liquid phase sintering aid to provide an additional pathway for ionic transport along grain boundaries. Considerable amounts of grain growth, in particular, and densification are required for the successful application of TGG, and no large difference in grain growth as a function of sintering atmosphere was noted in Figure 4.6, warranting the use of a liquid phase sintering aid.

Thermal profiles were chosen to promote a two-stage sintering approach: an initial stage in which samples were sintered with a Li_2O overpressure to maximally enable densification and a second stage where specimens were sintered in air to promote grain growth to fully texture the microstructure without entrapping a large amount of porosity. A similar approach has previously been reported to control oxygen vacancy concentration in two stages during sintering of $BaTiO_3$.[178,179] The temperatures and durations of the two different steps in the sintering process were varied to determine the best combination for achieving a dense, highly textured microstructure. The microstructures of two specimens with different sintering profiles are shown in Figure 4.10 below. The specimen pictured in Figure 4.10a was sintered first for ten minutes at 1300 °C, followed by a ten hour soak at 1250 °C, all of which occurred in a Li_2O-rich atmosphere. This profile follows a more traditional two-step sintering profile in that the first stage occurs at a higher temperature and is much shorter than the second, lower temperature stage.[178,179] The pictured surface shows multiple regions of abnormal grain growth. One region in particular, outlined by a dashed red line in the figure, is directly caused by texturing of the matrix particles by a seed crystal lying just below the surface of the polycrystalline part. The specimen in Figure 4.10b was initially subjected to a 1275 °C heat treatment in a Li_2O-rich atmosphere for twelve hours and a subsequent heat treatment of 1350 °C for

thirty hours in ambient air. This sintering profile was chosen to promote necking between particles without rapid grain growth in the first stage and emphasize grain growth in the second stage. A polished cross section of this sample is shown in Figure 4.10 and features a large grain that spans the entire thickness of the tape. This large grain is the result of templating of matrix powder by a seed crystal, outlined in red to show its original size. The pores present at the surface of the template are typical of ceramics produced via TGG.[167,168] Both of these samples exhibit microstructures that show evidence of templated grain growth.

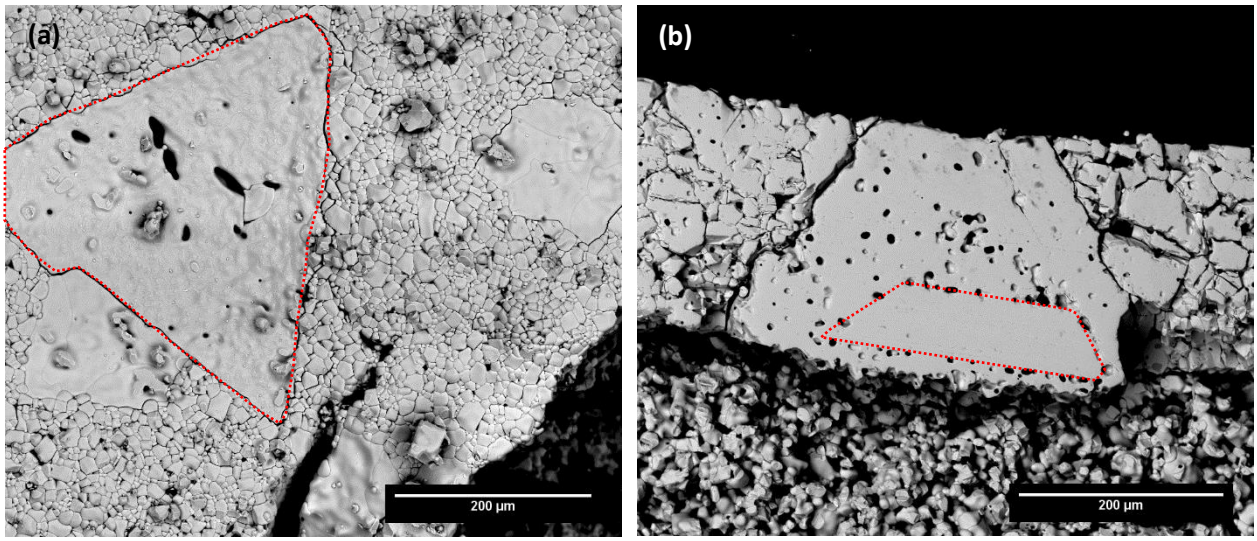

Figure 4.10: SEM micrographs of two $LiTaO_3$ polycrystals exhibiting templated grain growth from seeded ceramic tapes. The locations of the seed are emphasized with red lines for reference. (a) Sintered at 1350 °C for 10 minutes followed by a 10 hour soak at 1250 °C in a Li_2O-rich atmosphere. (b) Sintered for 12 hours at 1275 °C in a Li_2O-rich atmosphere and heat treated in an ambient atmosphere at 1350 °C for 30 hours.

Texturing of these samples was quantified by measuring X-ray diffraction profiles and by calculation of a Lotgering factor over the 2θ range of 15-70°. The XRD data from the most highly textured specimen made during this study, sintered at 1250 °C in Li_2O for 10 hours and then 1350 °C in air for 30 hours, is given in Figure 4.11. Although the seed crystals purchased from NanoLN possessed *z*-cut texture the intensity of the (0 0 6) lattice plane did not exhibit any signs of increased texture. Instead, the peak that increased in intensity the most is one corresponding to the (2 0 2) lattice plane with a Lotgering factor of 29%. The nature of this apparent change in texturing direction was not investigated.

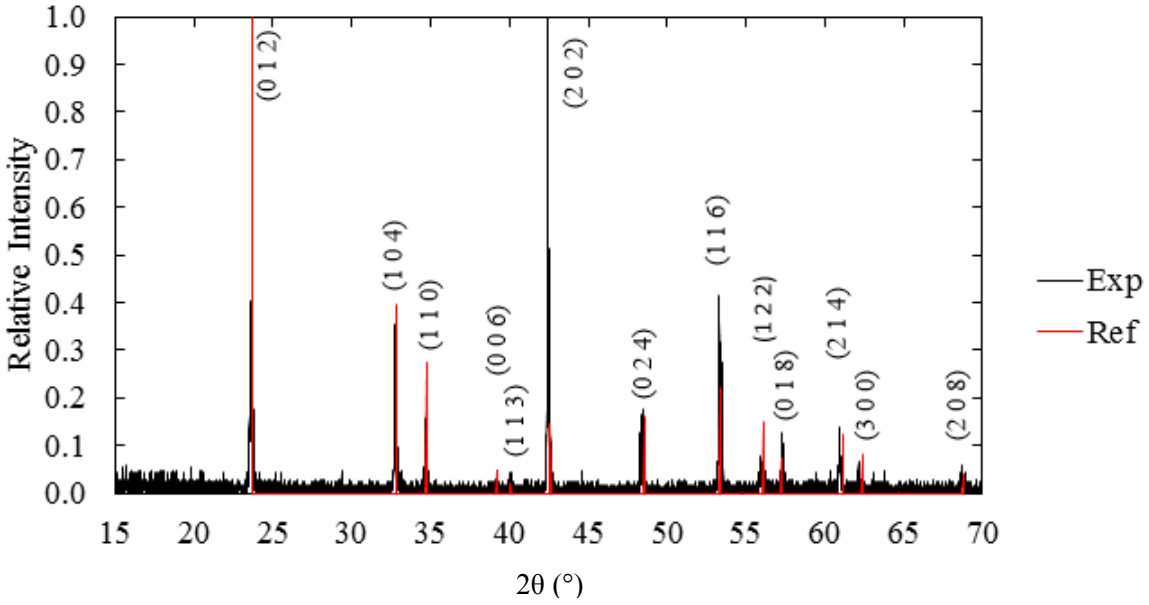

Fig. 4.11: X-ray diffraction data of a polycrystalline textured $LiTaO_3$ with (black) compared to a reference $LiTaO_3$ pattern that is randomly oriented. This sample, though seeded with *z*-cut templating crystals, shows 29% Lotgering factor in the (2 0 2) direction.

4.5 Summary

Adaptation of a VTE-like technique was used to control lithium volatilization and point defect concentrations in polycrystalline $LiTaO_3$ during sintering. Maintaining an overpressure of Li_2O vapor during sintering helped prevent lithium loss from the samples, as confirmed by the Curie temperature, and reduced the amount of lithium vacancies which likely act as diffusion pathways for tantalum ions during sintering. Randomly oriented sample sets that were sintered in an ambient air atmosphere contained a higher count of grains possessing intragranular porosity vs sample sets buried in a Li_2O vapor source. This is believed to be caused by the evolution of Li_2O from open pore surfaces during sintering, creating lithium vacancies that transport through the bulk of the grain and contribute to the non-densifying diffusion mechanism of lattice diffusion from a surface.

Atmosphere control, along with time and temperature adjustments, was used in a two-stage sintering approach to develop textured $LiTaO_3$ polycrystals. Templating of fine powder grains by large seed crystals was achieved and confirmed by electron microscopy and X-ray diffraction. Lotgering factor calculations showed that a low degree of texture was achieved, only 29%.

CHAPTER FIVE

CONCLUSIONS

Lithium tantalate exists in a wide solid solution chemistry range that, at lithium deficient compositions, possesses intrinsic lithium vacancies and tantalum antisite point defects. These defects, their removal, and their role in dominating material properties have been the subject of hundreds of studies throughout the last 40 years, yet specific questions have not been answered to date regarding: lithium diffusion in $LiTaO_3$ at high temperatures, how acoustic velocity is affected by point defects across the entire congruent-stoichiometric chemistry range, and what role point defect populations play in sintering of polycrystalline $LiTaO_3$.

Lithium diffusion coefficients in $LiTaO_3$ were determined for *z*-cut single crystals from the application of systematic confocal Raman spectroscopy to map lithium vacancy gradients through the thickness of the single crystals after partial VTE anneals. These data, along with temperature-dependent impedance sweeps, provide a way to measure the diffusion processes that are active during lithiation. A sample set of single crystals was developed based upon this information for further investigation into the role of point defects on thermal conductivity in this material system as a potential proxy for ferroelectric domain wall propagation. In bridging the entire solid solution chemistry range between the congruent and stoichiometric compositions of LT, it was found from frequency domain thermoreflectance and time domain thermoreflectance that thermal conductivity along the *z*-axis is 2x higher in stoichiometric LT than in congruent crystals due to scattering by $V_{Li}' + Ta_{Li}••••$ defect clusters. Inelastic neutron scattering experiments indicate that defect rich congruent $LiTaO_3$ possesses an acoustic velocity that is three times higher than stoichiometric $LiTaO_3$ along the *z*-axis. Direct measurement of the shear and longitudinal speed of sound in these single crystals showed that the longitudinal velocity is affected to a much greater degree (524 m/s difference between CLT and SLT) than the shear velocity (29 m/s difference between CLT and SLT).

The fabrication of polycrystalline lithium tantalate was explored in the first report of a pressureless, atmosphere-controlled technique designed to control defect populations and microstructure orientation. Application of a VTE-like technique to prevent lithium volatilization from polycrystalline LT was shown to avoid classic indicators of abnormal grain growth and qualitatively limit intragranular porosity. Templated grain growth, in conjunction with atmosphere control, was shown to be a viable method of texturing a polycrystalline LT microstructure to avoid CTE-induced stresses during sintering.

Lithium concentrations are of primary concern when discussing all aspects of forming $LiTaO_3$ and its properties. Calculation of diffusion coefficients via Raman spectroscopy provides a novel pathway for understanding intermediate steps of the VTE process. The impact of point defect concentrations on LT single crystals that bridge the congruent and stoichiometric compositions provide a point of contact between fundamental material properties and later studies of domain wall velocity, which is more heavily dependent on extrinsic factors. Discerning the role of point defect concentrations on densification and grain growth in polycrystalline specimens allows for diffusion mechanisms to be more finely controlled in future exploration of sintering this material.

CHAPTER SIX

SUGGESTED FUTURE WORKS

The studies discussed in this thesis laid a foundation for understanding the role that crystalline imperfections play in ferroelectric switching of lithium tantalate by producing sample sets that possessed controlled defect populations spanning the atomic scale to the micro scale. Additional studies could be performed by future researchers to confirm and expand upon the results outlined in Chapter 5. Suggestions for these future works are outlined in this chapter.

5.1 Intrinsic Point Defects

The confocal Raman technique developed in Chapter 2 examined phonon mode changes that were related to point defect concentrations to estimate lithium diffusion coefficients but did not explicitly measure lithium or lithium vacancy concentration profiles in the single crystals used for these experiments. Fourier transform infrared spectroscopy and x-ray photoelectron spectroscopy are tools that have been shown to be sensitive to lithium stoichiometry.[180–182] A series of surface measurements of Li concentration with either of these techniques followed by removal of a specified surface layer of VTI treated $LiTaO_3$ single crystals through an in situ sputtering ablation could provide quantifiable information on lithium concentrations for lithium diffusivity.

5.2 Acoustic Dynamics

The inelastic neutron scattering data presented in this document present an interesting trend, in that they suggest phonon velocities increase in this material as lithium vacancy and tantalum antisite defect concentrations increase. Measurement of additional phonon modes and a more complete sample set that bridges the congruent and stoichiometric chemistries is called for to fully investigate the effect of native point defect populations on acoustic phonon velocity in $LiTaO_3$.

Similarly, direct measurement of the speed of sound along different crystallographic axes could be measured in $LiTaO_3$ single crystals that have different orientations would be useful. VTE preparation of *x*- or *y*-cut samples would likely require longer duration VTI treatments than the *z*-cut crystals, however, because of the reported Li diffusivity differences between crystallographic axes.

The thermal conductivity techniques used in this work are generally limited to samples that are up to a few micrometers in thickness.[162,166] This leaves them more susceptible to surface-related effects than other methods of measuring thermal conductivity, like laser flash analysis, and in particular more affected by any chemical gradients that may reside near the surface of VTE treated lithium tantalate single crystals. Confirmation of thermal conductivity with a technique that measures further into the bulk of a sample would be prudent to confirm that there are no surface-related effects that dominate thermal conductivity signatures.

5.3 Polycrystalline, Textured $LiTaO_3$

The role of atmosphere type on densification and grain growth of polycrystalline $LiTaO_3$ is left with opportunity for future work. Sintering under vacuum would likely promote lithium oxide volatilization. O_2 and reducing atmospheres could have allowed for the effect of oxygen vacancy concentrations on sintering to be investigated.

Exploration of grain orientation and subsequent effects on polarization coupling across grain boundaries could be investigated through the development of $LiTaO_3$ bicrystals. The use of large bicrystals would allow for easy location of domain walls both nearby and far away from the grain boundary and make observation of domain wall movement under various experimental conditions more attainable.

REFERENCES CITED

1. Valasek, J. Piezo-Electric Activity of Rochelle Salt under Various Conditions. *Phys. Rev.* **19**, 478 (1922).

2. Lines, M. E. & Glass, A. M. *Principles and Applications of Ferroelectrics and Other Materials*. (Oxford University Press, 1977).

3. Lawless, W. N. 180° Domain-Wall Energies in BaTiO3. *Phys. Rev.* **175**, 619–624 (1968).

4. Merz, W. J. Domain Formation and Domain Wall Motions in Ferroelectric BaTiO3 Single Crystals. *Phys. Rev.* **95**, 690–698 (1954).

5. Goo, E. K. W., Mishra, R. K. & Thomas, G. Electron microscopy study of the ferroelectric domains and domain wall structure in PbZr0.52Ti0.48O3. *J. Appl. Phys.* **52**, 2940–2943 (1981).

6. Jesse, S. *et al.* Direct imaging of the spatial and energy distribution of nucleation centres in ferroelectric materials. *Nat. Mater.* **7**, 209–215 (2008).

7. Zhi, Y. *et al.* Phase mapping of domain kinetics in lithium niobate by digital holographic interferometry. *J. Appl. Phys.* **105**, (2009).

8. Nelson, C. T. *et al.* Domain dynamics during ferroelectric switching. *Science (80-.).* **334**, 968–972 (2011).

9. Lee, D. *et al.* Active Control of Ferroelectric Switching Using Defect-Dipole Engineering. *Adv. Mater.* **24**, 6490–6495 (2012).

10. Zeng, X. & Rajapakse, R. K. N. D. Eshelby tensor for piezoelectric inclusion and application to modeling of domain switching and evolution. *Acta Mater.* **51**, 4121–4134 (2003).

11. Moulson, A. J. & Herbert, J. M. *Electroceramics: Materials, Properties, Applications*. (John Wiley & Sons, Inc., 2003).

12. Zhu, W., Fujii, I., Ren, W. & Trolier-McKinstry, S. Domain Wall Motion in A and B Site Donor-Doped Pb(Zr0.52Ti0.48)O3 Films. *J. Am. Ceram. Soc.* **95**, 2906–2913 (2012).

13. Agronin, A., Rosenwaks, Y. & Rosenman, G. Direct observation of pinning centers in ferroelectrics. *Appl. Phys. Lett.* **88**, 2004–2007 (2006).

14. McGilly, L. J., Feigl, L. & Setter, N. Dynamics of ferroelectric 180° domain walls at engineered pinning centers. *Appl. Phys. Lett.* **111**, (2017).

15. Tybell, T., Paruch, P., Giamarchi, T. & Triscone, J. M. Domain Wall Creep in Epitaxial Ferroelectric Pb(Zr0.2Ti0.8)O3 Thin Films. *Phys. Rev. Lett.* **89**, 8–11 (2002).

16. Shin, Y.-H., Grinberg, I., Chen, I.-W. & Rappe, A. M. Nucleation and growth mechanism of ferroelectric domain-wall motion. *Nature* **449**, 881–884 (2007).

17. Padilla, J., Zhong, W. & Vanderbilt, D. First-principles investigation of 180° domain walls in BaTiO3. *Phys. Rev. B - Condens. Matter Mater. Phys.* **53**, R5969–R5973 (1996).

18. Miller, R. C. & Weinreich, G. Mechanism for the Sidewise Motion of 180° Domain Walls in Barium Titanate. *Phys. Rev.* **117**, 1460–1466 (1960).

19. Soergel, E. Piezoresponse force microscopy (PFM). *J. Phys. D. Appl. Phys.* **44**, (2011).

20. Daniels, J. E., Finlayson, T. R., Studer, A. J., Hoffman, M. & Jones, J. L. Time-resolved diffraction measurements of electric-field-induced strain in tetragonal lead zirconate titanate. *J. Appl. Phys.* **101**, (2007).

21. Daniels, J. E. *et al.* Two-step polarization reversal in biased ferroelectrics. *J. Appl. Phys.* **115**, 10–15 (2014).

22. Meng, Q. *et al.* Velocity of domain-wall motion during polarization reversal in ferroelectric thin films: Beyond Merz's Law. *Phys. Rev. B - Condens. Matter Mater. Phys.* **91**, 1–7 (2015).

23. Gopalan, V. *et al.* Mobility of 180° domain walls in congruent LiTaO3 measured using real-time electro-optic imaging microscopy. *J. Appl. Phys.* **86**, 1638–1646 (1999).

24. Jones, J. L., Kounga, A. B., Aulbach, E. & Granzow, T. Domain Switching During Electromechanical Poling in Lead Zirconate Titanate Ceramics. *J. Am. Ceram. Soc.* **91**, 1586–1590 (2008).

25. Jones, J. L., Pramanick, A. & Daniels, J. E. High-throughput evaluation of domain switching in piezoelectric ceramics and application to PbZr0.6Ti0.4O3 doped with La and Fe. *Appl. Phys. Lett.* **93**, 152904 (2008).

26. Porokhonskyy, V. & Damjanovic, D. Separation of piezoelectric grain resonance and domain wall dispersion in Pb(Zr,Ti)O3 ceramics. *Appl. Phys. Lett.* **94**, 212906 (2009).

27. Pramanick, A., Daniels, J. E. & Jones, J. L. Subcoercive cyclic electrical loading of lead zirconate titanate ceramics II: Time-resolved X-Ray diffraction. *J. Am. Ceram. Soc.* **92**, 2300–2310 (2009).

28. Pramanick, A., Damjanovic, D., Daniels, J. E., Nino, J. C. & Jones, J. L. Origins of Electro-Mechanical Coupling in Polycrystalline Ferroelectrics During Subcoercive Electrical Loading. *J. Am. Ceram. Soc.* **94**, 293–309 (2011).

29. Rojac, T., Kosec, M. & Damjanovic, D. Large Electric-Field Induced Strain in BiFeO3 Ceramics. *J. Am. Ceram. Soc.* **94**, 4108–4111 (2011).

30. Jones, J. L. *et al.* Domain wall and interphase boundary motion in a two-phase morphotropic phase boundary ferroelectric: Frequency dispersion and contribution to piezoelectric and dielectric properties. *Phys. Rev. B* **86**, 024104 (2012).

31. Tutuncu, G., Damjanovic, D., Chen, J. & Jones, J. L. Deaging and Asymmetric Energy Landscapes in Electrically Biased Ferroelectrics. *Phys. Rev. Lett.* **108**, 177601 (2012).

32. Page, K., Kolodiazhnyi, T., Proffen, T., Cheetham, A. K. & Seshadri, R. Local Structural Origins of the Distinct Electronic Properties of Nb-Substituted SrTiO3 and BaTiO3. *Phys. Rev. Lett.* **101**, 205502 (2008).

33. Roshchupkin, D. V., Irzhak, D. V. & Antipov, V. V. Study of LiNbO3 and LiTaO3 ferroelectric domain structures using high-resolution x-ray diffraction under application of external electric field. *J. Appl. Phys.* **105**, 024112 (2009).

34. Levin, I. *et al.* Local structure, pseudosymmetry, and phase transitions in Na1/2Bi1/2TiO3-K1/2Bi1/2TiO3. *Phys. Rev. B* **87**, 024113 (2013).

35. Korobko, R. *et al.* In-situ extended X-ray absorption fine structure study of electrostriction in Gd doped ceria. *Appl. Phys. Lett.* **106**, 042904 (2015).

36. Yazawa, K., Ducharne, B., Uchida, H., Funakubo, H. & Blendell, J. E. Barkhausen noise analysis of thin film ferroelectrics. *Appl. Phys. Lett.* **117**, 012902 (2020).

37. Shur, V. Y. *et al.* Barkhausen Jumps During Domain Wall Motion in Ferroelectrics. *Ferroelectrics* **267**, 347–353 (2002).

38. Shur, V. Y., Akhmatkhanov, A. R., Baturin, I. S. & Shishkina, E. V. Polarization reversal and jump-like domain wall motion in stoichiometric LiTaO3 produced by vapor transport equilibration. *J. Appl. Phys.* **111**, (2012).

39. Akhmatkhanov, A. R., Kipenko, I. A., Esin, A. A. & Shur, V. Y. Barkhausen pulses caused by domain merging in congruent lithium niobate. *Appl. Phys. Lett.* **117**, 022903 (2020).

40. Miller, R. C. Some Experiments on the Motion of 180° Domain Walls in BaTiO3. *Phys. Rev.* **111**, 736–739 (1958).

41. Rudyak, V. M., Kudzin, A. Y. & Panchenko, T. V. Barkhausen jumps and stabilization of spontaneous polarization of BaTiO3 single-crystals. *Sov. Phys. Solid State* **14**, (1973).

42. Mayergoyz, I. D. The classical Preisach model of hysteresis and reversibility. *J. Appl. Phys.* **69**, 4602–4604 (1991).

43. Bartic, A. T., Wouters, D. J., Maes, H. E., Rickes, J. T. & Waser, R. M. Preisach model for the simulation of ferroelectric capacitors. *J. Appl. Phys.* **89**, 3420–3425 (2001).

44. Fujii, I. F., Hong, E. H. & Trolier-McKinstry, S. Thickness dependence of dielectric nonlinearity of lead zirconate titanate films. *IEEE Trans. Ultrason. Ferroelectr. Freq. Control* **57**, 1717–1723 (2010).

45. Ovchinnikov, O. *et al.* Local measurements of Preisach density in polycrystalline ferroelectric capacitors using piezoresponse force spectroscopy. *Appl. Phys. Lett.* **96**, 10–13 (2010).

46. Monnor, T., Laosiritaworn, Y. & Yimnirun, R. Towards a better understanding of relationship between preisach densities and polarization reversals on hysteresis characteristic. *Adv. Condens. Matter Phys.* **2013**, (2013).

47. Damjanovic, D. & Demartin, M. The Rayleigh law in piezoelectric ceramics. *J. Phys. D. Appl. Phys.* **29**, 2057–2060 (1996).

48. Schenk, T. *et al.* Physical Approach to Ferroelectric Impedance Spectroscopy: The Rayleigh Element. *Phys. Rev. Appl.* **10**, 1–12 (2018).

49. Eitel, R. E. Rayleigh Law Response in Ferroelectric Ceramics: Quantifying Domain Wall Dynamics and Structural Relationships. *2007 Sixt. IEEE Int. Symp. Appl. Ferroelectr.* 319–323 (2007). doi:10.1109/ISAF.2007.4393253

50. Trolier-McKinstry, S., Bassiri Gharb, N. & Damjanovic, D. Piezoelectric nonlinearity due to motion of 180° domain walls in ferroelectric materials at subcoercive fields: A dynamic poling model. *Appl. Phys. Lett.* **88**, 202901 (2006).

51. Dierolf, V. & Koerdt, M. Combined excitation-emission spectroscopy of Er3+ ions in stoichiometric LiNbO3: The site selectivity of direct and up conversion excitation processes. *Phys. Rev. B* **61**, 8043–8052 (2000).

52. Dierolf, V., Sandmann, C., Kim, S., Gopalan, V. & Polgar, K. Ferroelectric domain imaging by defect-luminescence microscopy. *J. Appl. Phys.* **93**, 2295–2297 (2003).

53. Sandmann, C. & Dierolf, V. The role of defects in light induced domain inversion in lithium niobate. *Phys. status solidi* **2**, 136–140 (2005).

54. Dierolf, V., Capek, P. & Sandmann, C. Luminescence and Raman Based Real Time Imaging of Ferroelectric Domain Walls. *MRS Proc.* **966**, 0966-T08-03 (2006).

55. Dierolf, V. & Sandmann, C. Combined excitation emission spectroscopy of defects for site-selective probing of ferroelectric domain inversion in lithium niobate. *J. Lumin.* **125**, 67–79 (2007).

56. Dierolf, V., Sandmann, C. & Capek, P. Defect based real-time diagnostics of ferroelectric domain wall motion. *Phys. Status Solidi* **204**, 690–694 (2007).

57. Gopalan, V., Dierolf, V. & Scrymgeour, D. A. Defect – Domain Wall Interactions in Trigonal Ferroelectrics. *Annu. Rev. Mater. Res.* **37**, 449–489 (2007).

58. Stone, G., Knorr, B., Gopalan, V. & Dierolf, V. Frequency shift of Raman modes due to an applied electric field and domain inversion in LiNbO3. *Phys. Rev. B* **84**, 134303 (2011).

59. Kitamura, K., Furukawa, Y., Niwa, K., Gopalan, V. & Mitchell, T. E. Crystal growth and low coercive field 180° domain switching characteristics of stoichiometric LiTaO3. *Appl. Phys. Lett.* **73**, 3073–3075 (1998).

60. Gopalan, V. & Mitchell, T. E. Wall velocities, switching times, and the stabilization mechanism of 180° domains in congruent LiTaO3 crystals. *J. Appl. Phys.* **83**, 941–954 (1998).

61. Kim, S., Gopalan, V., Kitamura, K. & Furukawa, Y. Domain reversal and nonstoichiometry in lithium tantalate. *J. Appl. Phys.* **90**, 2949–2963 (2001).

62. Kim, S., Gopalan, V. & Gruverman, A. Coercive fields in ferroelectrics: A case study in lithium niobate and lithium tantalate. *Appl. Phys. Lett.* **80**, 2740–2742 (2002).

63. Tian, L., Gopalan, V. & Galambos, L. Domain reversal in stoichiometric LiTaO3 prepared by vapor transport equilibration. *Appl. Phys. Lett.* **85**, 4445–4447 (2004).

64. Jach, T., Kim, S., Gopalan, V., Durbin, S. & Bright, D. Long-range strains and the effects of applied field at 180° ferroelectric domain walls in lithium niobate. *Phys. Rev. B* **69**, (2004).

65. Choudhury, S. *et al.* The influence of 180° ferroelectric domain wall width on the threshold field for wall motion. *J. Appl. Phys.* **104**, 6–8 (2008).

66. Hum, D. S. *et al.* Optical properties and ferroelectric engineering of vapor-transport-equilibrated, near-stoichiometric lithium tantalate for frequency conversion. *J. Appl. Phys.* **101**, (2007).

67. Salje, E. K. H., Wang, X., Ding, X. & Scott, J. F. Ultrafast Switching in Avalanche-Driven Ferroelectrics by Supersonic Kink Movements. *Adv. Funct. Mater.* **27**, (2017).

68. Smyth, D. M. Defects and transport in LiNbO 3. *Ferroelectrics* **50**, 93–102 (1983).

69. Lerner, P., Legras, C. & Dumas, J. P. Stoechiométrie des monocristaux de métaniobate de lithium. *J. Cryst. Growth* **3**–**4**, 231–235 (1968).

70. Abrahams, S. C. & Marsh, P. Defect Structure Dependence on Composition in Lithium Niobate. *Acta Crystalographia* **B42**, 61–68 (1986).

71. Iyi, N. *et al.* Comparative Study of Defect Structures in Lithium Niobate with Different Compositions. *J. Solid State Chem.* 340–352 (1992).

72. Wilkinson, A. P., Cheetham, A. K. & Jarman, R. H. The defect structure of congruently melting lithium niobate. *J. Appl. Phys.* **74**, 3080–3083 (1993).

73. Zotov, N., Boysen, H., Frey, F., Metzger, T. & Born, E. Cation substitution models of congruent LiNbO3 investigated by X-ray and neutron powder diffraction. *J. Phys. Chem. Solids* **55**, 145–152 (1994).

74. DeLeo, G. G., Dobson, J. L., Masters, M. F. & Bonjack, L. H. Electronic structure of an oxygen vacancy in lithium niobate. *Phys. Rev. B* **37**, 8394–8400 (1988).

75. Shannon, R. D. Revised Effective Ionic Radii and Systematic Studies of Interatomic Distances in Halides and Chalcogenides. *Acta Crystalographia* **A32**, 751–767 (1976).

76. Donnerberg, H., Tomlinson, S. M., Catlow, C. R. A. & Schirmer, O. F. Computer-simulation studies of extrinsic defects in LiNbO3 crystals. *Phsyical Rev. B* **44**, 4877–4883 (1991).

77. Schirmer, O. F., Theimann, O. & Wohlecke, M. Defects in LiNbO3 - I. Experimental Aspects. *J. Phys. Chem. Solids* **52**, 185–200 (1991).

78. Ivanova, E. M., Sergeev, N. A. & Yatsenko, A. V. Analysis of intrinsic defects in the lithium niobate structure by the NMR Li-7 method. *Crystallogr. Reports* **43**, 337 (1998).

79. Yatsenko, A. V., Ivanova, E. N. & Sergeev, N. A. NMR study of intrinsic defects in congruent LiNbO3. 1. 'Unoverlapping' defects. *Phys. B* **240**, 254–262 (1997).

80. Zhdanov, G. S., Kolontsova, E. V., Korneev, A. E. & Ivanov, S. A. X-ray diffuse scattering from single crystal LiNbO3 and LiTaO3 as a function of temperature between 20–750°C. *Ferroelectrics* **21**, 463–465 (1977).

81. Ivanov, S. A., Korneev, A. E., Kolontsova, E. V. & Venevtsev, Y. N. Temperature dependence of intensity of diffuse X-ray scattering in single crystals of LiTaO3. *Krystallografiya* **23**, 1071–1073 (1978).

82. Zotov, N. *et al.* X-ray and Neutron Diffuse Scattering in LiNbO3 from 38 to 1200 K. *Acta Crystalographia* **B51**, 477–488 (1995).

83. Abdi, F., Fontana, M. D., Aillerie, M. & Bourson, P. Coexistence of Li and Nb vacancies in the defect structure of pure LiNbO3 and its relationship to optical properties. *Appl. Phys. A* **83**, 427–434 (2006).

84. Li, Y.-Y. *et al.* Investigation of the defect structure of congruent and Fe-doped LiNbO3 powders synthesized by the combustion method. *Materials (Basel).* **10**, 380 (2017).

85. Li, Y., Schmidt, W. G. & Sanna, S. Intrinsic LiNbO3 point defects from hybrid density functional calculations. *Phys. Rev. B* **89**, (2014).

86. Kim, S., Gopalan, V., Kitamura, K. & Furukawa, Y. Domain reversal and nonstoichiometry in lithium tantalate. *J. Appl. Phys.* **90**, 2949–2963 (2001).

87. Xu, H. *et al.* Structure and diffusion of intrinsic defect complexes in LiNbO3 from density functional theory calculations. *J. Phys. Condens. Matter* **22**, (2010).

88. Peterson, G. E. & Carruthers, J. R. 93Nb NMR as a Sensitive and Accurate Probe of Stoichiometry in LiNbO3 Crystals. *J. Solid State Chem.* **1**, 98–99 (1969).

89. Carruthers, J. R., Peterson, G. E., Grasso, M. & Bridenbaugh, P. M. Nonstoichiometry and Crystal Growth of Lithium Niobate. *J. Appl. Physics1* **42**, 1846–1851 (1971).

90. Gopalan, V. & Gupta, M. C. Observation of internal field in LiTaO3 single crystals: Its origin and time-temperature dependence. *Appl. Phys. Lett.* **68**, 888 (1995).

91. Kitamura, K., Yamamoto, J. K., Iyi, N., Kimura, S. & Hayashi, T. Stoichiometric LiNbO3 single crystal growth by double crucible Czochralski method using automatic powder supply system. *J. Cryst. Growth* **116**, 327–332 (1992).

92. Kitamura, K., Furukawa, Y., Niwa, K., Gopalan, V. & Mitchell, T. E. Crystal growth and low coercive field 180° domain switching characteristics of stoichiometric LiTaO3. *Appl. Phys. Lett.* **73**, 3073–3075 (1998).

93. Gopalan, V., Mitchell, T. E., Furukawa, Y. & Kitamura, K. The role of nonstoichiometry in 180° domain switching of LiNbO3 crystals. *Appl. Phys. Lett.* **72**, 1981–1983 (1998).

94. Gopalan, V. & Gupta, M. C. Observation of internal field in LiTaO3 single crystals: its origin and time-temperature dependence. *Appl. Phys. Lett.* **68**, 888–890 (1996).

95. Gopalan, V., Aust, J. A., Sanford, N. A., Kitamura, K. & Furukawa, Y. Crystal growth, characterization, and domain studies in ferroelectric lithium niobate and tantalate. in *Handbook of Advanced Electronic and Photonic Materials and Devices* (ed. Nalwa, H. S.) 57–114 (Academic, 2000).

96. Tsuya, H. Optical damage in transition-metal-doped LiTaO3. *J. Appl. Phys.* **46**, 4323–4333 (1975).

97. Hum, D. Frequency conversion in near-stoichiometric lithium tantalate fabricated by vapor transport equilibration. (Stanford University, 2007).

98. Nakamura, M., Takekawa, S. & Kitamura, K. Anisotropy of thermal conductivities in non- and Mg-doped near-stoichiometric LiTaO3 crystals. *Opt. Mater. (Amst).* **32**, 1410–1412 (2010).

99. Kitamura, K., Takekawa, S., Nakamura, M., Kurimura, S. & Louchev, O. Defect density dependence of thermal conductivity and temperature control of quasi-phasematching devices. in *2005 Quantum Electronics and Laser Science Conference* 900–903 (2005).

100. Scott, B. A. & Burns, G. Determination of Stoichiometry Variations in LiNbO3 and LiTaO3 by Raman Powder Spectroscopy. *J. Am. Ceram. Soc.* **55**, 225–230 (1972).

101. Kostritskii, S. M., Aillerie, M., Bourson, P. & Kip, D. Raman spectroscopy study of compositional inhomogeneity in lithium tantalate crystals. *Appl. Phys. B* **95**, 125–130 (2009).

102. Fontana, M. D. & Bourson, P. Microstructure and defects probed by Raman spectroscopy in lithium niobate crystals and devices. *Appl. Phys. Rev.* **2**, 040602 (2015).

103. Ridah, A., Bourson, P., Fontana, M. D. & Malovichko, G. The composition dependence of the Raman spectrum and new assignment of the phonons in LiNbO3. *J. Phys. Condens. Matter* **9**, 9687–9693 (1997).

104. Shi, L. *et al.* The composition dependence and new assignment of the Raman spectrum in lithium tantalate. *Solid State Commun.* **135**, 251–256 (2005).

105. Kostritskii, S. M., Bourson, P., Aillerie, M., Fontana, M. D. & Kip, D. Quantitative evaluation of the electro-optic effect and second-order optical nonlinearity of lithium tantalate crystals of different compositions using Raman and infrared spectroscopy. *Appl. Phys. B Lasers Opt.* **82**, 423–430 (2006).

106. Ballman, A. A., Levinson, H. J., Capio, C. D. & Brown, H. Curie temperature and birefringence variation in ferroelectri lithium metatantalate as a function of melt stoichiometry. *J. Am. Ceram. Soc.* **50**, 657–659 (1967).

107. Furukawa, Y., Kitamura, K., Suzuki, E. & Niwa, K. Stoichiometric LiTaO3 single crystal growth by double crucible Czochralski method using automatic powder supply system. *J. Cryst. Growth* **197**, 889–895 (1999).

108. Bordui, P. F., Norwood, R. G., Bird, C. D. & Carella, J. T. Stoichiometry issues in single-crystal lithium tantalate. *J. Appl. Phys.* **78**, 4647–4650 (1995).

109. Bäumer, C. *et al.* Composition dependence of the ultraviolet absorption edge in lithium tantalate. *J. Appl. Phys.* **93**, 3102–3104 (2003).

110. Carruthers, J. R., Kaminow, I. P. & Stulz, L. W. Diffusion Kinetics and Optical Waveguiding Properties of Outdiffused Layers in Lithium Niobate and Lithium Tantalate. *Appl. Opt.* **13**, 2333–2342 (1974).

111. Torii, Y., Sekiya, T., Yamamoto, T., Koyabashi, K. & Abe, Y. Preparation and properties of LiTaO3-based solid solutions with cation vacancies. *Mater. Res. Bulliten* **18**, 1569–1574 (1983).

112. Shah, R. R., Kim, D. M., Rabson, T. A. & Tittel, F. K. Characterization of iron-doped lithium niobate for holographic storage applications. *J. Appl. Phys.* **47**, 5421–5431 (1976).

113. Ohkubo, Y., Saito, T., Murakami, Y., Yokoyama, A. & Kawase, Y. Behavior of Impurities In and Cd in the LiNbO 3–LiTaO 3 System. *Mater. Trans.* **43**, 1469–1474 (2002).

114. Grabmaier, B. C., Wersing, W. & Koestler, W. Properties of undoped and MgO-doped LiNbO3; correlation to the defect structure. *J. Cryst. Growth* **110**, 339–347 (1991).

115. Grabmaier, B. C. & Otto, F. Growth and investigation of MgO-doped LiNbO3. *J. Cryst. Growth1* **79**, 682–688 (1986).

116. Nakamura, M. *et al.* Refractive indices in undoped and MgO-doped near-stoichiometric LiTaO3 crystals. *Japanese J. Appl. Physics, Part 2 Lett.* **41**, (2002).

117. Clark, M. G., DiSalvo, F. J., Glass, A. M. & Peterson, G. E. Electronic structure and optical index damage of iron-doped lithium niobate. *J. Chem. Phys.* **59**, 6209–6219 (1973).

118. Xue, D. & He, X. Dopant occupancy and structural stability of doped lithium niobate crystals. *Phys. Rev. B* **73**, 7 (2006).

119. Zhang, Z. & Xue, D. Local Lattice Structure and Dopant Occupancy of Doped Lithium Niobate Crystals. *Mod. Phys. Lett. B* **23**, 3687–3694 (2009).

120. Volk, T. & Wohlecke, M. *Lithium Niobate: Defects, Photorefraction and Ferroelectric Switching*.

121. Chen, C.-F. *et al.* Processing of crack-free high density polycrystalline LiTaO3 ceramics. *J. Mater. Sci. Mater. Electron.* **28**, 3725–3732 (2017).

122. Zhang, Y., Yao, Y. & He, S. Sinterability and dielectric properties of LiTaO3-based ceramics with addition of CoO. *Materials (Basel).* **13**, (2020).

123. Chen, C.-F. *et al.* Powder Synthesis and Hot-Pressing of a LiTaO3 Ceramic. *J. Am. Ceram. Soc.* **95**, 2820–2826 (2012).

124. Shimada, S., Kodaira, K. & Matsushita, T. Sintering LiTaO3 and KTaO3 with the aid of manganese oxide. *J. Mater. Sci.* **19**, 1385–1390 (1984).

125. Ye, Z. G., Von Der Muhll, R. & Ravez, J. Sintering Mechanism of LiTaO3 Ceramics by the Addition of Lithium and Magnesium Fluorides. in *1990 IEEE 7th International Symposium on*

Applications of Ferroelectrics 566–569 (1990).

126. Malovichko, G., Grachev, V. & Schirmer, O. Interrelation of intrinsic and extrinsic defects – congruent, stoichiometric, and regularly ordered lithium niobate. *Appl. Phys. B* **68**, 785–793 (1999).

127. Margueron, S. *et al.* Resolved E-symmetry zone-centre phonons in LiTaO3 and LiNbO3. *J. Appl. Phys.* **104105**, (2012).

128. Caciuc, V., Postnikov, A. V & Borstel, G. Ab initio structure and zone-center phonons in LiNbO3. *Phys. Rev. B* **61**, 8806–8813 (2000).

129. Mendes-Filho, J., Lemos, V. & Cerdelra, F. Pressure dependence of the Raman spectra of LiNbO3 and LiTaO3. *J. Raman Spectrosc.* **15**, 367–369 (1984).

130. Kong, Y. *et al.* Ilmenite-like stacking defect in nonstoichiometric lithium niobate crystals investigated by Raman scattering spectra. *J. Appl. Phys.* **87**, 4410–4414 (2000).

131. Nassau, K. & Lines, M. E. Stacking-fault model for stoichiometry deviations in LiNbO3 and LiTaO3 and the effect on the curie temperature. *J. Appl. Phys.* **41**, 533–537 (1970).

132. Balluffi, R. W., Allen, S. M. & Carter, W. C. *Kinetics of Materials*. (John Wiley & Sons, Inc., 2005).

133. Yang, J. *et al.* Twin defects in thick stoichiometric lithium tantalate crystals prepared by a vapor transport equilibration method. *J. Cryst. Growth* **433**, 31–35 (2016).

134. Vere, A. W. Mechanical twinning and crack nulceation in lithium niobate. *J. Mater. Sci.* **3**, 617–621 (1968).

135. Park, B. M., Kitamura, K., Furukawa, Y. & Ji, Y. Relation between mechanical twinning and cracking in stoichiometric lithium niobate single crystals. *J. Am. Ceram. Soc.* **80**, 2689–2692 (1997).

136. Zhang, D.-L., Wang, Z., Hua, P.-R. & Pun, E. Y.-B. Li-Rich Vapor Transport Equilibration Temperature Dependence of Surface Composition of Initially Congruent LiNbO3 Crystal. *J. Am. Ceram. Soc.* **95**, 2798–2800 (2012).

137. Chen, B., Hua, P.-R., Zhang, D.-L. & Pun, E. Y.-B. Stoichiometry Dependence of Li+ Diffusivity in LiNbO3 Crystal in Off-Congruent, Li-Deficient Regime. *J. Am. Ceram. Soc.* **95**, (2011).

138. Li, Q. *et al.* Lithium Diffusion in Lithium Niobate Crystals with Different Initial Li2O Content at High Temperature. *J. Am. Ceram. Soc.* **99**, 3055–3059 (2016).

139. Chin, G. Y., Ballman, A. A., Tien, P. K. & Riva-Sanseverino, S. Diffusion kinetics and optical quality in LiNbO3-LiTaO3 optical waveguides. *Appl. Phys. Lett.* **26**, 637–639 (1975).

140. Chowdhury, M. R., Peckham, G. E., Ross, R. T. & Saunderson, D. H. Lattice dynamics of lithium niobate. *J. Phys. C Solid State Phys.* **7**, L99–L102 (1974).

141. Scrymgeour, D. A., Gopalan, V., Itagi, A., Saxena, A. & Swart, P. J. Phenomenological theory of a single domain wall in uniaxial trigonal ferroelectrics: Lithium niobate and lithium tantalate. *Phys. Rev. B - Condens. Matter Mater. Phys.* **71**, 1–13 (2005).

142. Abrahams, S. C. & Bernstein, J. L. Ferroelectric Lithium Tantalate - I. Single crystal X-ray diffraction study at 24 °C. *J. Phys. Chem. Solids* **28**, 1685–1692 (1967).

143. Langenberg, E. *et al.* Analysis of the temperature dependence of the thermal conductivity of insulating single crystal oxides. *APL Mater.* **4**, (2016).

144. Yang, J., Long, J. & Yang, L. First-principles investigations of the physical properties of lithium niobate and lithium tantalate. *Phys. B Phys. Condens. Matter* **425**, 12–16 (2013).

145. Cheng, G. *et al.* Inelastic neutron scattering of lithium tantalate studied in the ferroelectric and paraelectric phases. *J. Phys. Condens. Matter* **5**, 2707–2718 (1993).

146. Friedrich, M., Schindlmayr, A., Schmidt, W. G. & Sanna, S. LiTaO3 phonon dispersion and ferroelectric transition calculated from first principles. *Phys. Status Solidi B* **689**, 683–689 (2016).

147. Abrahams, S. C., Buehler, E., Hamilton, W. C. & Laplaca, S. J. Ferroelectric Lithium Tantalate - III. Temperature dependence of the structure in the ferroelectric phase and the paraelectric structure at 940 K. *J. Phys. Chem. Solids* **34**, 521–532 (1973).

148. Sakuma, T. & Nakxyama, T. A Comment on Phonon Mass Defect Scattering. *Lett. Al Nuovo Cim.* **2**, 701–706 (1971).

149. Agrawal, B. K. Scattering of long-wavelength phonons by point defects in cubic lattices. *J. Phys. C Solid State Phys.* **2**, 252–258 (1969).

150. Agrawal, B. K. Phonon Scattering by Line Defects. *Phys. Rev. B* **3**, 1843–1856 (1971).

151. Schwartz, J. W. & Walker, C. T. Phonon Scattering By Lattice Vacancies. *Phys. Rev. Lett.* **16**, 97–98 (1966).

152. Caldwell, R. F. & Klein, M. V. Experimental and Theoretical Study of Phonon Scattering from Simple Point Defects in Sodium Chloride. *Phys. Rev.* **158**, 851–875 (1967).

153. Harrington, J. A. & Walker, C. T. Phonon Scattering by Point Defects in CaF2, SrF2, and BaF2. *Phys. Rev. B* **1**, 882–890 (1970).

154. Walker, C. T. & Pohl, R. O. Phonon Scattering by Point Defects. *Phys. Rev.* **131**, 1433–1442 (1963).

155. Chau, C.-K. & Klein, M. V. Phonon Scattering from Substitutional Impurities and Lattice Defects in Silver Chloride. *Phys. Rev. B* **1**, 2642–2660 (1970).

156. Klemens, P. G. The thermal conductivity of dielectric solids at low temperatures. *Proc. R. Soc. Lond. A* **208**, 108–133 (1951).

157. Pichanusakorn, P. & Bandaru, P. Nanostructured thermoelectrics. *Mater. Sci. Eng. R* **67**, 19–63 (2010).

158. Toberer, E. S., Zevalkink, A. & Snyder, G. J. Phonon engineering through crystal chemistry. *J. Mater. Chem.* **21**, 15843–15852 (2011).

159. Fankhauser, H. R. Dynamics of Crystals with Molecular Impurity Centers. II. Resonance Scattering of Lattice Waves. *Phys. Rev. B* **8**, 4475–4486 (1973).

160. Yao, M. *et al.* Phonon-defect scattering in doped silicon by molecular dynamics simulation. *J. Appl. Phys.* **104**, (2008).

161. Scott, E. A. *et al.* Phonon scattering effects from point and extended defects on thermal conductivity studied via ion irradiation of crystals with self-impurities. *Phys. Rev. Mater.* **2**, 095001 (2018).

162. Schmidt, A. J., Cheaito, R. & Chiesa, M. A frequency-domain thermoreflectance method for the characterization of thermal properties. *Rev. Sci. Instrum.* **80**, (2009).

163. Cahill, D. G. Analysis of heat flow in layered structures for time-domain thermoreflectance. *Rev. Sci. Instrum.* **75**, 5119 (2004).

164. Touloukia, Y. S. & Byco, E. H. *Thermophysical properties of matter - the TPRC data series. Volume 4. Specific heat - metallic elements and alloys*. (1971).

165. Nakamura, M., Takekawa, S., Liu, Y. & Kitamura, K. Growth and characterization of Sc-doped near-stoichiometric LiTaO3 cyrstals. *J. Cryst. Growth* **311**, 272–277 (2009).

166. Cheaito, R., Gorham, C. S., Misra, A., Hattar, K. & Hopkins, P. E. Thermal conductivity measurements via time-domain thermoreflectance for the characterization of radiation induced damage. *J. Mater. Res.* **30**, 1403–1412 (2015).

167. Messing, G. L. *et al.* Templated Grain Growth of Textured Piezoelectric Ceramics. *Crit. Rev. Solid State Mater. Sci.* 45–96 (2004). doi:10.1080/10408430490490905

168. Meier, W. *et al.* Highly Textured BaTiO3 via Templated Grain Growth and Resulting Polarization Reversal Dynamics. *J. Am. Ceram. Soc.* **99**, 922–929 (2016).

169. Lotgering, F. K. Topotactical Reactions with Ferrimagnetic Oxides Having Hexagonal Crystal Structures. *J. Inorg. Nucl. Chem.* **9**, 113–123 (1959).

170. Seabaugh, M. M., Vaudin, M. D., Cline, J. P. & Messing, G. L. Comparison of Texture Analysis Techniques for Highly Oriented a-Al2O3. *J. Am. Ceram. Soc.* **83**, 2049–2054 (2000).

171. Jones, J. L., Slamovich, E. B. & Bowman, K. J. Critical Evaluation of the Lotgering Degree of Orientation Texture Indicator. *J. Mater. Res.* **19**, 3414–3422 (2011).

172. Rahaman, M. N. *Ceramic Processing and Sintering*. (Marcel Dekker, Inc, 2003).

173. Fielitz, P. *et al.* Tantalum and niobium diffusion in single crystalline lithium niobate. *Solid State Ionics* **259**, 14–20 (2014).

174. Birnie, D. P. & Bordui, P. F. Defect-based description of lithium diffusion into lithium niobate. *J. Appl. Phys.* **76**, 3422–3428 (1994).

175. Barns, R. L. & Carruthers, J. R. Lithium Tantalate Single Crystal Stoichiometry. *J. Appl. Crystallogr.* **3**, 395–399 (1970).

176. Bordui, P. F., Norwood, R. G., Jundt, D. H. & Fejer, M. M. Preparation and characterization of off-congruent lithium niobate crystals. *J. Appl. Phys.* **71**, 875–879 (1992).

177. Kingon, A. I. & Clark, J. B. Sintering of PZT Ceramics: I, Atmosphere Control. *J. Am. Ceram. Soc.* **66**, 253–256 (1982).

178. Zhao, Q., Gong, H., Wang, X., Chen, I. W. & Li, L. Superior Reliability Via Two-Step Sintering: Barium Titanate Ceramics. *J. Am. Ceram. Soc.* **99**, 191–197 (2016).

179. Polotai, A., Breece, K., Dickey, E., Randall, C. & Ragulya, A. A novel approach to sintering nanocrystalline barium titanate ceramics. *J. Am. Ceram. Soc.* **88**, 3008–3012 (2005).

180. Aurback, D., Weissman, I., Schechter, A. & Cohen, H. X-ray Photoelectron Spectroscopy Studies of Lithium Surfaces Prepared in Several Important Electrolyte Solutions. A Comparison with Previous Studies by Fourier Transform Infrared Spectroscopy. *Langmuir* **12**, 3991–4007 (1996).

181. Shutthanandan, V. *et al.* Application of XPS in the characterization of Battery materials. *J. Electron Spectros. Relat. Phenomena* (2018). doi:10.1016/j.elspec.2018.05.005

182. Meyer, L., Curran, D., Brow, R., Santhanagopalan, S. & Porter, J. Operando Measurements of Eletrolyte Li-ion Concentration during fast charging with FTIR/ATR. *J. Electrochem. Soc.* **168**, (2021).

183. Ivy, J. M., Song, Y., Choi, S. & Brennecka, G. L. Thermal conductivity within the solid solution chemistry range of LiTaO3. *Appl. Phys. Lett.* (2022).

APPENDIX

A.1 Broader Impacts

The primary purpose of graduate school is to prepare a new researcher to independently identify an open-ended scientific question, plan a series of experiments to solve the problem or fill the information gap, and execute those experiments. While learning how to address these steps in the research process, a graduate student is typically presented with opportunities to develop other personal and professional skills that can be beneficial to the student and greater community across a wide array of aspects. The author of this thesis would like to expand upon some of the opportunities for a broader, community-wide impact that they were fortunate to take part in throughout their PhD experience at Colorado School of Mines (Mines).

As a graduate student, the author of this thesis had the opportunity to mentor and teach 16 undergraduate and high school students in the ways of ceramic and glass science and processing. Several of these students have gone on to gainful employment or graduate school themselves. This proved to be a personally very satisfying endeavor despite a relative lack of productive research accomplished.

The author functioned as instrumental component in the formation of a Keramos chapter at Mines. Keramos is a national professional fraternity whose mission is to promote and emphasize scholarship and character in the thoughts of students in ceramics, to stimulate mental development, and to promote interest in the professional aspects of ceramic engineering, technology, and science. In establishing a Keramos chapter at Mines, the undergraduate students within the Metallurgical and Materials Engineering department that are particularly interested in ceramics and glass could access resources specifically geared toward their interests.

Hands-on learning and experimentation is an invaluable tool in the toolbox of any engineer or scientist. The thesis writer was able to increase the capability for Mines students of all disciplines to garner some of this personal experience by designing and building a glassblowing studio and structuring a course for undergraduate students to learn hot glass working. Equipment for the studio was researched, purchased,

and installed on an initial equipment and materials budget of approximately $30,000. Personal instruction of the first two generations of gaffers (a.k.a. glassblowers) and development of the structure of the laboratory course transpired between August and November of 2017. As of August 2021, over 100 students have completed the Art and Science of Glassblowing course. Management was transitioned to Keramos to provide the undergraduates with an opportunity to develop their own leadership, managerial, and technical skills. The role of Glass Shop Manager has since been held by six different students who have been responsible for performing equipment maintenance, scheduling and executing workshops and sales to provide funding for glassworking supplies, maintaining the list of approved users, and managing open shop time so that the users may continue to safely expand upon their skills after they are beyond the class setting.

The ability to contribute to the Mines community and expand upon the education opportunities of so many students has been uniquely enjoyable. Personal mentorships, providing resources for students interested in ceramics and glass, and expanding the footprint for hands-on scientific and artistic exploration at an institution are not opportunities that all graduate students are presented with, and the author is thankful to have been able to participate in them.

A.2 Supplemental Materials

Permissions for reprinted content in Figures 1.7, 3.4, 3.5, 3.7, 4.2, and 4.3 can be found in the Supplemental Materials for this document.